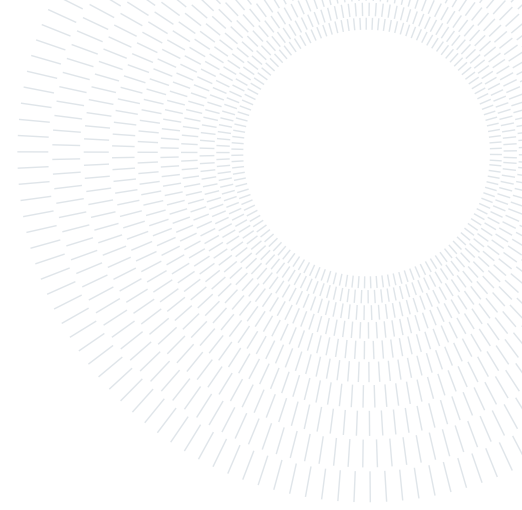




POLITECNICO
MILANO 1863

SCUOLA DI INGEGNERIA INDUSTRIALE
E DELL'INFORMAZIONE



An AI-Enhanced Model of Athermal Fission Gas Release in SCIANTIX

TESI DI LAUREA MAGISTRALE IN

NUCLEAR ENGINEERING - INGEGNERIA NUCLEARE

Arianna Pagani, 995999

Advisor:

Prof. Davide Pizzocri

Co-advisors:

Giovanni Zullo

Lelio Luzzi

Academic year:

2022-2023

Abstract: The surge in interest surrounding low-temperature phenomena calls for the description of athermal fission gas behaviour. This holds particular significance for reactors operating in such conditions, including certain Small Modular Reactor designs and fast neutron reactors employing fuels with high thermal conductivity, such as nitride fuels. Additionally, its implications extend to the context of spent fuel storage conditions. In this work, an AI-enhanced physics-based model of the athermal fission gas behaviour is presented, extending mechanistic models available in the open literature. The athermal release, defined as the fraction of gas vented from the fuel through its open porosity, is accounted for via the solution of the gas diffusion within the fuel grain, evaluating the fraction of the concentration gradient in the proximity of grain edges. The results of such computation are included in the SCIANTIX code thanks to a dedicated neural network, aimed at encapsulating the complex dependencies affecting the athermal release, whilst ensuring a computational time in line with fuel performance applications. Additionally, in the context of this analysis, semi-empirical models for solid fission products swelling and fuel densification were incorporated as well, both relevant phenomena in low-temperature conditions. The consistency of the model is tested with data available in the literature.

Key-words: low-temperature applications, fission gas release, athermal fission gas behaviour, SCIANTIX, artificial intelligence, neural network

1. Introduction

Investigating the behaviour of nuclear fuel rods under irradiation is one of the fundamental activities required for the safe design, licensing and operation of nuclear reactors. Additionally, such investigations hold significance for studies concerning final repositories [1]. This necessitates a comprehensive understanding of the various phenomena impacting fuel performance under irradiation.

One such crucial aspect is the behavior of fission gases, particularly Xenon and Krypton. On one hand, fission gases precipitate into bubbles resulting in fuel swelling, which promotes pellet-cladding gap closure and the ensuing pellet-cladding mechanical interaction (PCMI) [2]. On the other hand, fission gas release (FGR) to the fuel rod free volume causes pressure build-up and thermal conductivity degradation of the rod filling gas [3]. The release of fission products from irradiated fuel is generally considered to be controlled by atomic diffusion to the fuel grain boundaries [4]. Several mechanisms of fission gas release exist that are relevant in different conditions and across different temperature ranges. At high temperatures the thermal diffusion of fission gas

dominates. At moderate temperatures, the irradiation-enhanced defect concentrations drive the fission gas diffusion, whereas at low temperatures, the athermal contribution is most relevant.

The athermal fission gas release holds prime importance in reactors that operate at low temperatures, e.g some designs of small modular reactors (SMRs), and, also, for fast neutron reactors using fuels with high thermal conductivity, such as nitride fuels¹. In the latter, the release may not be as strong as at higher temperatures in oxide fuels but still enough to degrade the gap conductance [5]. Furthermore, the contribution of athermal fission gas release could be significant for spent fuel storage conditions [6]. Various mechanisms of athermal fission gas release exist. These may occur via recoil or knockout mechanisms or be induced by the presence of open channels in the fuel matrix. This study specifically focuses on the latter one. The features of the open pore phase structure are such that the pores may be approximated by a continuous cylinder along the three-grain edges of the polyhedrons that make up the fuel structure. The as-fabricated porosity, which decreases during irradiation due to densification, contributes to the system of open tunnels of porosity at the grain edges, providing an easy escape path for gas atoms produced within the fuel grains. This system of percolated networks framing the grain is referred to as open porosity and it can be visualized in Figure 1.

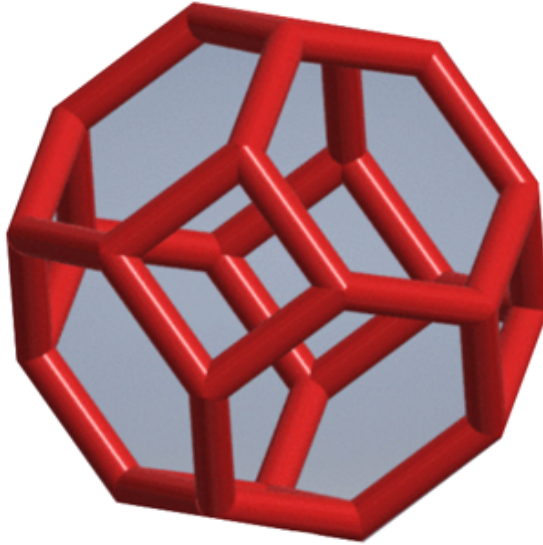


Figure 1: Visualization of the open porosity tunnels.

While Figure 1 provides a general depiction of the structure of the open porosity tunnels, it is essential to recognize that not all of these continuous cylinders representing the open porosity are interconnected, and the framework is not fully contiguous. Additionally, it is worth noting that a fraction of the open porosity exists as single pores that are connected at the surface of the pellet. This can be attributed to an anisotropic effect inherent in the relationship between fabrication porosity and open porosity. This phenomenon will be discussed in more detail in Section 2.

Numerous endeavors have been undertaken to characterise athermal fission gas behaviour, encompassing diverse methodologies from purely empirical approaches (e.g [7]) to the exploration of percolation phenomenon along grain boundaries [8, 9]. If the former oversimplifies the phenomenon, the latter approach seems rather hard to implement in a fuel performance code (FPC) since the grains and, therefore, the boundaries are usually not modelled individually. Instead, a model considering the open porosity as a mean-field quantity was developed by Caisse and Van Uffelen[10]. Nonetheless, although Claisse and Van Uffelen had accounted for the impact of open porosity on inter-granular fission gas release, their model is expected to over-predict FGR. Indeed, the athermal venting factor was described in their work as a purely geometrical quantity. The fuel grain was treated as spherical in shape, therefore, neglecting the effects of the shape of the gas concentration gradient along the grain edge and the inclination of the grain angle — factors influencing the actual fraction of gas reaching the open tunnel of porosity and, consequently, exiting.

The scope of this investigation is to present a physics-based modelling of the athermal fission gas behaviour, extending the mechanistic model developed in [10] and including machine learning (ML) applications, encapsulating the complex dependencies affecting the athermal release of fission gas diffusing in the fuel grain, whilst ensuring a computational time in line with fuel performance applications.

¹While our focus remains on UO_2 in this study, the model can be readily adapted for application with other fuel types.

It is worth noting that numerous other phenomena play a crucial role in fuel behavior in low-temperature applications, particularly solid swelling. Furthermore, as mentioned earlier, the fraction of open porosity resulting from fabrication porosity undergoes densification as the fuel is irradiated, affecting the network of open tunnels, which ultimately shrinks, impacting the fraction of athermal venting. Section 3 tackles these additional connected phenomena.

Moreover, for an accurate assessment of FGR to be conducted, it is essential that the process of release and retention of fission gases is properly understood. In lightly irradiated fuel, a significant presence of small, discrete, lenticular bubbles along the grain boundaries has been observed. As irradiation progresses, these bubbles evolve into elongated pores, eventually reaching the grain edges where three grains meet. This progression can lead to the formation of continuous pathways to the fuel exterior through which the gases may be vented. The final stage in the process is the inter-connection of all the porosity on the grain faces to the grain edges and from this point, all gas arriving at the boundaries will be released. However, the presence of fabrication porosity, as previously explained, ensures that some of these interconnected pathways are established from the incipit of fuel operation, leading to athermal release. A crucial determinant in this understanding is the kinetics of grain-face bubble development, with particular focus on grain-face swelling and bubble morphology. These aspects are heavily dependent on the value of grain boundary vacancy diffusivity. To effectively account for these phenomena, the model proposed by White [11] was chosen.

All aspects and models developed in this work have been integrated into the SCIANTIX code [12]. SCIANTIX is an open-source, 0-D meso-scale code, that describes inert gas behavior in nuclear fuel. To accurately incorporate the athermal contribution of FGR, new routines were introduced into the SCIANTIX code. These include an algorithm to evaluate the fraction of open porosity and a dedicated neural network designed to address athermal venting. Additionally, semi-empirical models were incorporated to account for solid swelling and porosity densification.

These enhancements enable SCIANTIX to provide a comprehensive understanding of the complex processes involved in athermal FGR within nuclear fuel, improving its predictive capabilities, especially in base irradiation cases.

The consistency and predictive capabilities of the model are tested using data available in the literature. Specifically, a separate effect test was conducted to assess the performance of SCIANTIX, augmented by the AI-enhanced model, by employing the Kashibe [13] and Baker [14] cases as benchmark scenarios. Furthermore, experimental data on fission gas release from base irradiation cases is utilized to estimate the model's behaviour studying scenarios used for the integral validation of SCIANTIX. Notably, the base irradiation cases from experiments AN3[15], REGATE, HATAC-C2 [16], and CONTACT1[17] are examined comprehensively to evaluate the model's predictive performance across various experimental conditions.

2. Methodology

In this section, a physics-based model for athermal fission gas release, built upon the framework established by the mechanistic model developed by Claisse and Van Uffelen is presented. Furthermore, to address the intricate dependencies influencing this phenomenon, whilst ensuring a computational time in line with fuel performance applications, we leverage artificial intelligence techniques. To achieve this, a synthetic dataset from a high-fidelity finite element methods code - responsible for solving the diffusion equation - is generated and consequently employed to train a feed-forward neural network.

2.1. Model development

The athermal fission gas release can be regarded as a venting process. This involves the release of gas by subtracting a portion of the gas concentration at grain boundaries, indicated as q (at m^{-3}), resulting from diffusion and governed by Equation 1. This specific fraction is defined as the athermal venting factor (f_{ath}).

$$\frac{\partial q}{\partial t} = (1 - f_{\text{ath}}) \left(D \frac{\partial c}{\partial r} \Big|_{r=a} \right) - R \quad (1)$$

where: D (m^2s^{-1}) is the single-atom diffusivity, a (m) is the spherical grain radius, c (at m^{-3}) is single-atom gas concentration and R (at $\text{m}^{-3} \text{s}^{-1}$) is the released rate.

The definition of the athermal venting factor, as proposed in [10], stems from the geometric characteristics of the grain, represented as a tetrakaidecahedron (TKD). It is expressed as the ratio between the surface of the open porosity tunnels (S_{op}) and the total surface of the TKD (S_{TKD}).

$$f_{\text{ath}} := \frac{S_{\text{op}}}{S_{TKD}} \quad (2)$$

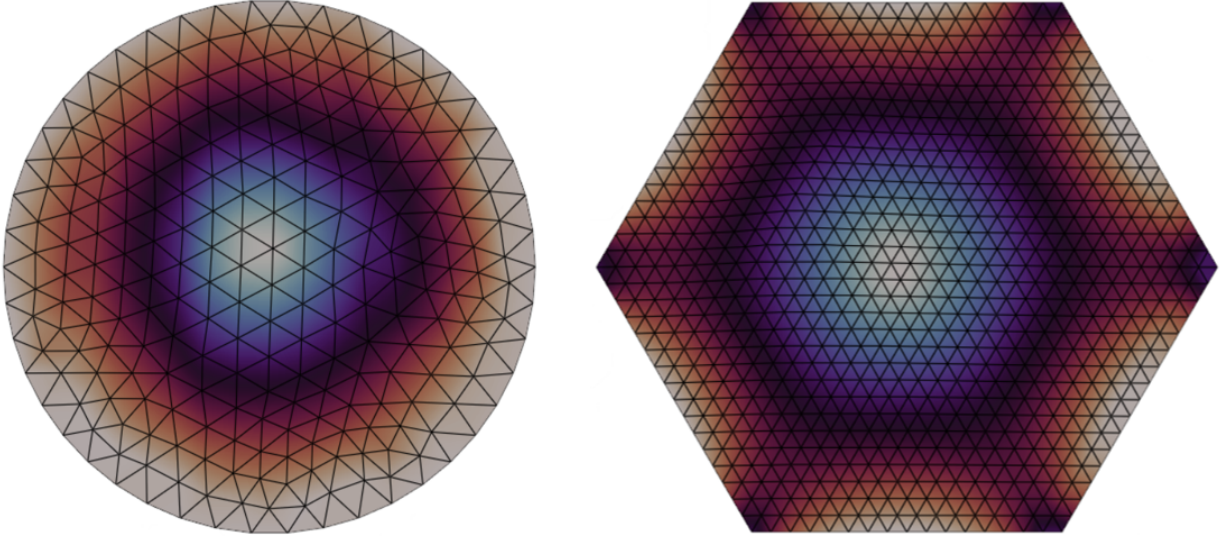
For a TKD characterized by an edge length l (m), a cylindrical porosity with a radius r (m) and P_{op} denoting the open porosity, the aforementioned ratio is evaluated as follows:

$$\frac{S_{\text{op}}}{S_{TKD}} = \frac{12}{1 + 2\sqrt{3}} \frac{r}{l} = 1.54\sqrt{P_{\text{op}}} \quad (3)$$

The initial open porosity is mainly situated at the pellet periphery. Nonetheless, it can be assumed to be uniformly distributed in the pellet, since the latter will crack after the first start-up, entailing the opening of a fraction of the initially closed porosity in the pellet. P_{op} is determined in [10] as a function of the fabrication porosity from an empirical linear fit inferred from the work of Song et. al [18] as:

$$\begin{cases} P_{\text{op}} = P_{\text{fab}}/20 & \text{Under 5\% of porosity} \\ P_{\text{op}} = 3.10P_{\text{fab}} - 0.1525 & \text{Under 5.8\% of porosity} \\ P_{\text{op}} = P_{\text{fab}}/2.1 - 3.2 & \text{Above 5.8\% of porosity} \end{cases} \quad (4)$$

As previously stated, this methodology assumes a uniform gas flux diffusing from within the grain, disregarding the actual geometry in which the diffusion occurs and, consequently, over-predicting the gas flux that reaches the grain edge where the open porosity is located. As it can be understood from Figure 2b, considering a hexagonal section of a TKD, and solving the diffusion equation within this domain would reveal a clear cosine-shaped pattern in the gas concentration gradient along the edges².



(a) Gas concentration gradient in a spherical domain.

(b) Gas concentration gradient in a hexagonal domain.

Figure 2: Comparison between the gas diffusion within a section of a sphere and within a section of a tetrakaidecahedron

Thus, the effective fraction of gas that arrives at the edge and enters in the open porosity tunnel appears to be notably smaller with respect to the spherical case assumed by Claisse and Van Uffelen, which can be visualised in Figure 2a.

In order to account for the real shape of the gas flux, including its dependency on the grain-edge inclination angle (θ), a corrective factor λ_{ath} for f_{ath} was defined, such that Equation 1 can be rewritten as:

$$\frac{\partial q}{\partial t} = (1 - f_{\text{ath}}\lambda_{\text{ath}}) \left(D \frac{3}{a} \frac{\partial c}{\partial r} \Big|_{r=a} \right) - R \quad (5)$$

²It is worth noting that, when moving from the spherical geometry to the hexagonal one, the conservation of a number of quantity must be upheld. In particular, as the Turnbull diffusion coefficient is retrieved from direct measures of $D \left(\frac{s}{v} \right)^2$, one should impose that the ratio $\frac{s}{v}$ is conserved transitioning from one geometry to another. Nonetheless, considering, on one side, that multiple atomistic studies (e.g. [19]) have confirmed the existence of an intrinsic D compatible with the one measure by Turnbull and, on the other, that in this work D is taken as a mere numerical parameter, decoupled from the model used to retrieve it, this balance was neglected.

This factor represents the ratio between the average integral flux exiting from the grain within the radius of the open porosity tunnel ($\langle \varphi^{\text{out}} \rangle_{\text{op}}$) and the total average integral exiting flux ($\langle \varphi^{\text{out}} \rangle_{\text{tot}}$).

$$\lambda_{\text{ath}} := \frac{\langle \varphi^{\text{out}} \rangle_{\text{op}}}{\langle \varphi^{\text{out}} \rangle_{\text{tot}}} \quad (6)$$

where:

$$\begin{cases} \langle \varphi^{\text{out}} \rangle_{\text{op}} = -\frac{2}{r} \int_r D \nabla c(x, y, t) dx dy \\ \langle \varphi^{\text{out}} \rangle_{\text{tot}} = -\frac{1}{l} \int_l D \nabla c(x, y, t) dx dy \end{cases} \quad (7)$$

Here, the specific value of r depends from P_{op} and can be retrieved inverting Equation 3.

$$r = 1.54 \sqrt{P_{\text{op}}} \frac{1 + 2\sqrt{3}}{12l} \quad (8)$$

To achieve a more physical interpretation of the relationship between P_{op} and P_{fab} the linear interpolation inferred by Claisse and Van Uffelen was replaced by a new semi-empirical fit (Figure 3), leading to the functional form:

$$P_{\text{op}} = \alpha P_{\text{fab}} + \frac{a}{1 + e^{-c(P_{\text{fab}} - b)}} \quad (9)$$

where $a = 2.8(\%)$, $b = 5.5(\%)$, $c = 5$ and $\alpha = \frac{1}{20}$.

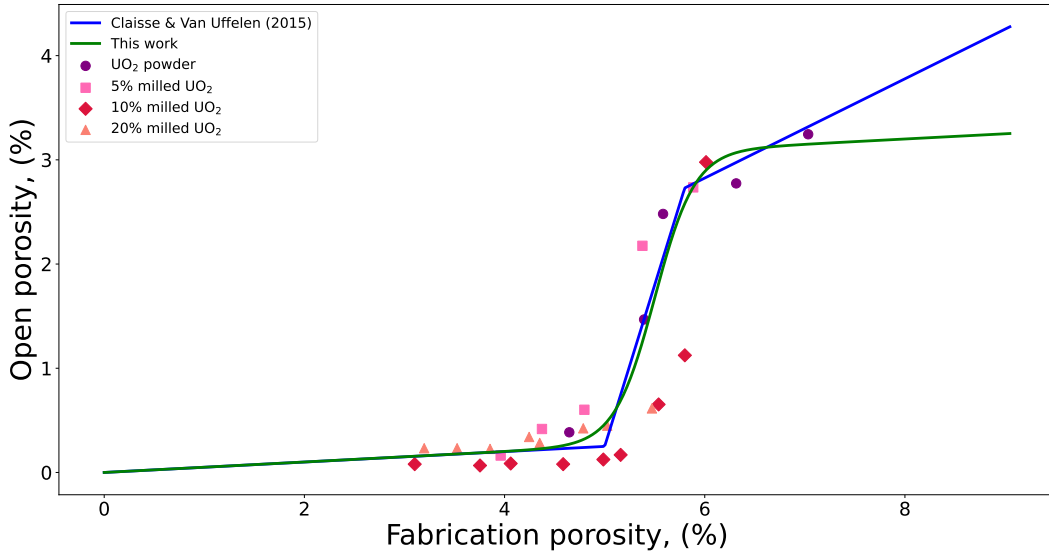


Figure 3: Comparison between this work's fit with the one inferred by Claisse and Van Uffelen [10]

The ODE from which the solution of Equation 11 stems can be expressed as:

$$\frac{dP_{\text{op}}}{dP_{\text{fab}}} = \alpha - \frac{c}{a} (P_{\text{op}} - \alpha P_{\text{fab}}) (a - P_{\text{op}} + \alpha P_{\text{fab}}) \quad (10)$$

Here we can highlight the relation between P_{op} and P_{fab} as the co-occurrence of two effects. The first one is isotropic in nature and characterized by the linear term of Equation 11. The second one, on the other side, is anisotropic and possibly explainable by a percolation mechanism that occurs at a threshold value of P_{fab} .

$$P_{\text{op}} = \underbrace{\alpha P_{\text{fab}}}_{\text{Isotropic term}} + \underbrace{\frac{a}{1 + e^{-c(P_{\text{fab}} - b)}}}_{\text{Anisotropic term}} \quad (11)$$

As densification progresses, the open porosity initially shrinks proportionally with respect to the fabrication porosity. This initial behavior reflects the gradual closure of individual open pores. However, a critical point

might be reached where the interconnected network of open tunnels collapses. This collapse might be driven by mechanisms related to percolation theory, where the interconnected pathways become severed. Following this, the relationship between open and fabrication porosity transitions to a linear behavior again. This could be explained by the fact that the remaining open pores become isolated.

Coming back to the computation of λ_{ath} , this requires a thorough understanding of the underlying diffusion dynamics and the effect induced by variations of θ . To address this, it was imperative to select a spatial domain comprehensive enough to account for the variable dependence on θ .

Initially, a 3D representation of the grain was selected. This involved choosing a quarter of the hexagonal section of the TKD as the domain, exploiting the symmetry of diffusion within the grain. However, due to the nature of the 3D representation essentially being an extruded 2D model and the additional numerical complexities it introduced, it was decided to transition to a 2D representation. With these considerations in mind, it was deemed appropriate to choose a rhomboidal portion from the hexagon resulting in a section of the TKD as the reference domain, as depicted in Figure 4.

In Appendix A, an analytical exploration of gas diffusion within our designated domain is discussed. Nevertheless, tackling the solution of a partial differential equation (PDE) in a complex 2D geometry, as encountered here, poses considerable challenges. In particular, the dependence on θ In Appendix A, an analytical exploration of gas diffusion within our designated domain is discussed. Nevertheless, tackling the solution of a partial differential equation (PDE) in a complex 2D geometry, as encountered here, poses considerable challenges. In particular, beside the presence of non-standard coordinate systems, the boundary conditions of the domain may vary with θ , adding another layer of complexity. Specifying and integrating these variable boundary conditions into the solution process requires careful consideration and may necessitate specialized mathematical treatment. Thus, recognizing the need for a robust computational method to tackle the complexity of the diffusion problem, a numerical approach was embraced, employing finite element methods (FEM). The diffusion equation within the aforementioned domain was solved using the software MATLAB [20], specifically its PDE toolbox. The PDEModel Objects were employed, encapsulating the problem’s essential aspects: defining the mesh as a θ -dependent geometry and enforcing symmetry boundary conditions along the axes and null concentration along the boundaries S_1 and S_2 (Figure 4). The factor λ_{ath} was calculated as an averaged value between the ratio in Equation 6 computed on surfaces S_1 and S_2 , depicted in Figure 4.

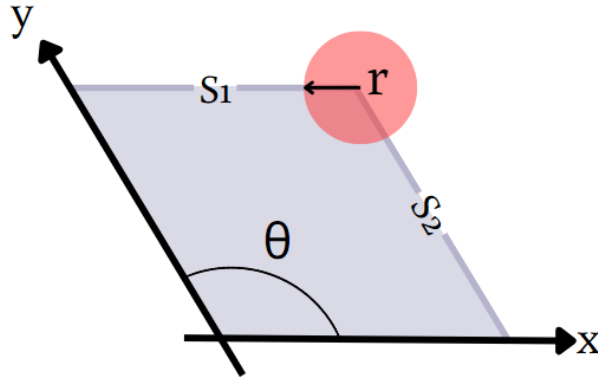


Figure 4: Generic domain representing a section of the tetrakaidecahedron in grey and highlighting the presence of the open porosity tunnel in red.

Conducting a sensitivity analysis on the computed value of λ_{ath} in relation to the mesh coarseness revealed minimal variation. Numerous scenarios were explored by altering the target maximum mesh edge length H_{max} , while maintaining all other parameters affecting gas diffusion constant. Across 12 evaluated cases, spanning from a maximum value of $H_{\text{max}} = 1\% \cdot l \approx 0.44 \mu\text{m}$ to a minimum value of $10\% \cdot r \approx 0.0385 \mu\text{m}$, the observed standard deviation relative to the mean of λ_{ath} was found to be 6.81×10^{-5} . Although an analytical comparison to the FEM code’s computed value is unavailable, this result suggests a high level of fidelity for the code. Ultimately, the chosen value for H_{max} was set as $0.5 \cdot r \approx 0.192 \mu\text{m}$.

2.2. AI-Enhanced Model

In Section 2, the fundamental underlying physical conceptualization of our work was presented. As previously stated a corrective factor with respect to the original formulation envisioned by Claisse and Van Uffelen was introduced, accounting for the solution of the diffusion equation in a domain dependent on the grain-edge inclination angle. A high-fidelity code, written in MATLAB, was employed to solve the diffusion equation

and provide us with a value for λ_{ath} depending on the grain-inclination angle (θ), the fabrication porosity (P_{fab}), the grain edge length (l), the burn-up (β), the temperature (T) and the gas generation rate (\dot{F}) and gas initial concentration (C_0). Of particular importance is the effect of the grain-edge inclination angle θ on the shape of the gas diffusion gradient and, ultimately, on the athermal venting factor. To gain a comprehensive understanding of this influence, the initial step involved examining the range of this angle.

Based on observations from scanning electron microscope (SEM) images of nuclear fuel grains, as shown in Figure 5, we inferred a validity range spanning from 90 to 135 degrees³.

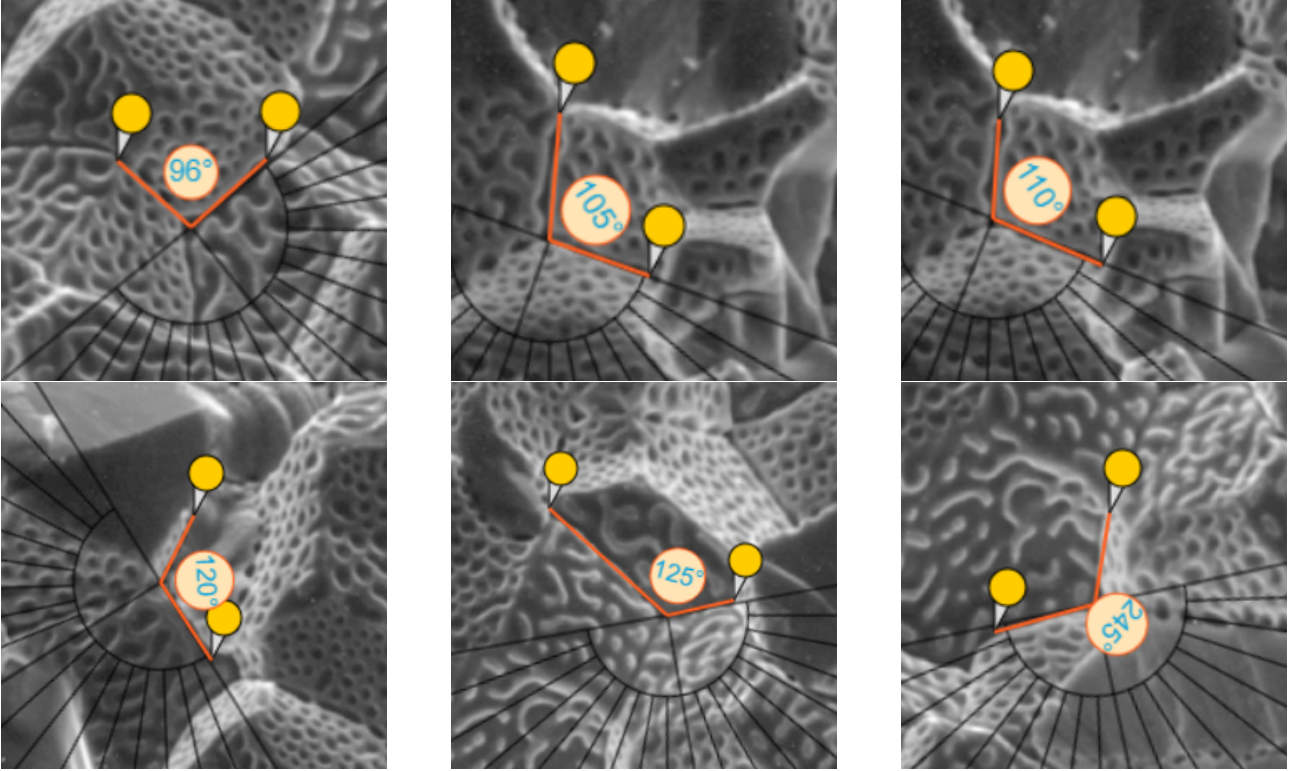


Figure 5: Collection of SEM images highlighting the range in values of the grain inclination θ in UO_2 (Images from [21]). The range of validity of the grain-edge inclination angle can be observed to stay within an interval that goes, approximately, from 90° to 135° . It is noted that, while evaluating angles in a 2-D representation of a 3-D object may introduce some minor discrepancies, these are assumed to be insignificant. It's also highlighted that the grain-edge inclination angle is not an independent quantity; rather, it must adhere to the constraint that, intuitively, the sum of the three angles at a three-grain-edge junction equals 360° .

Taking into consideration these specified values, we performed simulations to observe the behavior of gas diffusion across various geometries. Figure 6 serves as a visual representation of our observations. Notably, when the angle becomes exceptionally steep, such as when $\theta = 90^\circ$, the process of gas diffusion is hindered at the grain's edge. Consequently, the concentration gradient at this juncture remains low. Given that the flux exiting the grain is directly proportional to the concentration gradient, this, in turn, as illustrated in Figure 6a, translates to a small amount of gas being able to exit and enter the tunnel of open porosity positioned at the edge.

As θ increases, the gradient within the tunnel of porosity grows. Furthermore, the shape of the concentration gradient within the grain progressively changes, gradually becoming more uniform. Eventually, as θ approaches 135° , a notable phenomenon occurs: the gradients present on surfaces S1 and S2 (with reference to Figure 4) converge and merge together. This convergence marks a critical point where the distribution of gas concentration within the grain reaches a high level of homogeneity, resembling the trend present in a circular geometry instead, the same uniformity is depicted in Figure 2a.

³It should be noted that the value of θ depends from the orientation of the three-grain junction lines.

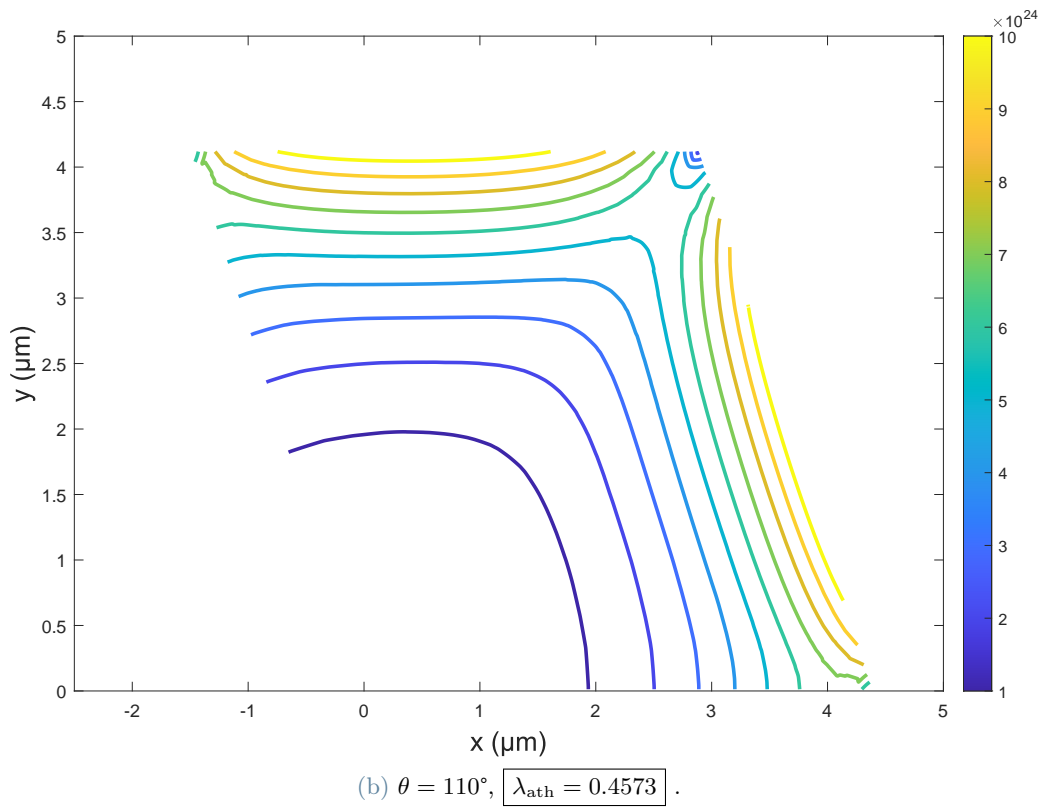
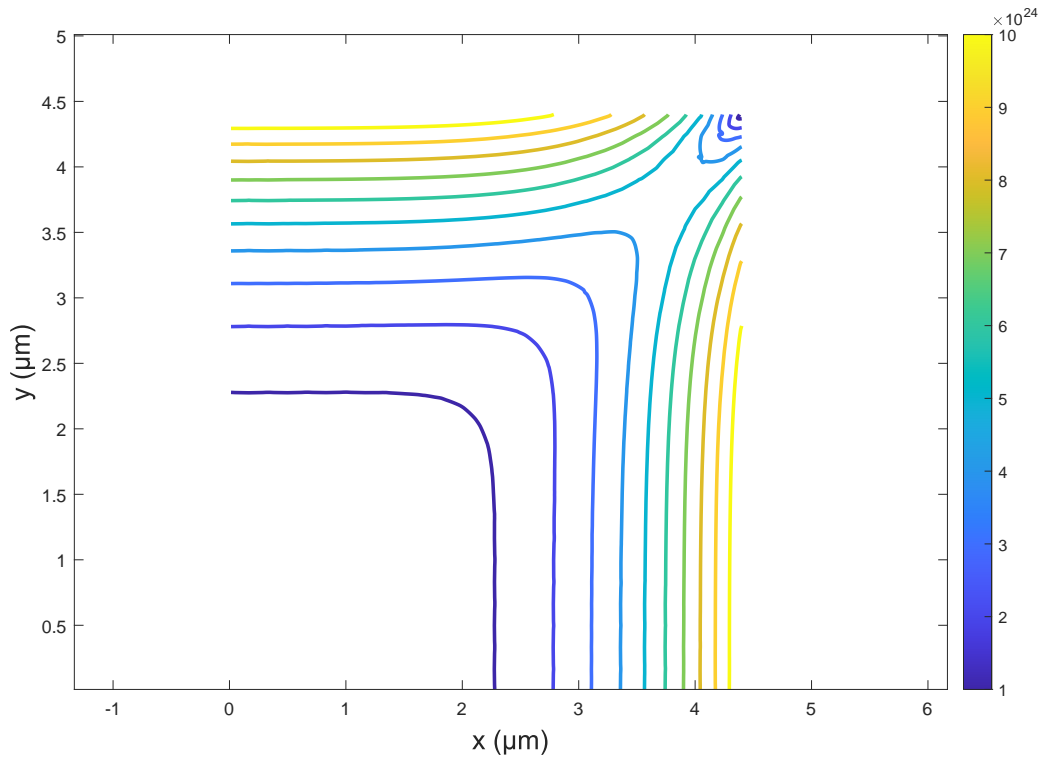


Figure 6: Comparison of the gas diffusion gradient shape with respect to the grain-edge inclination angle.

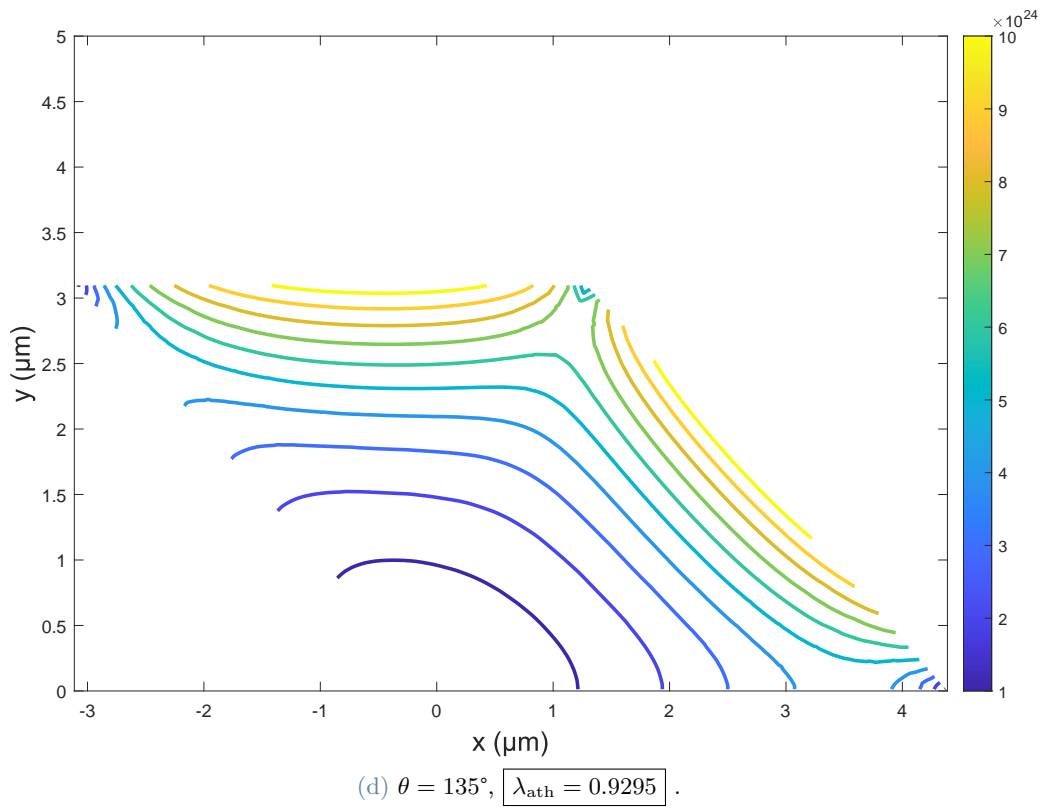
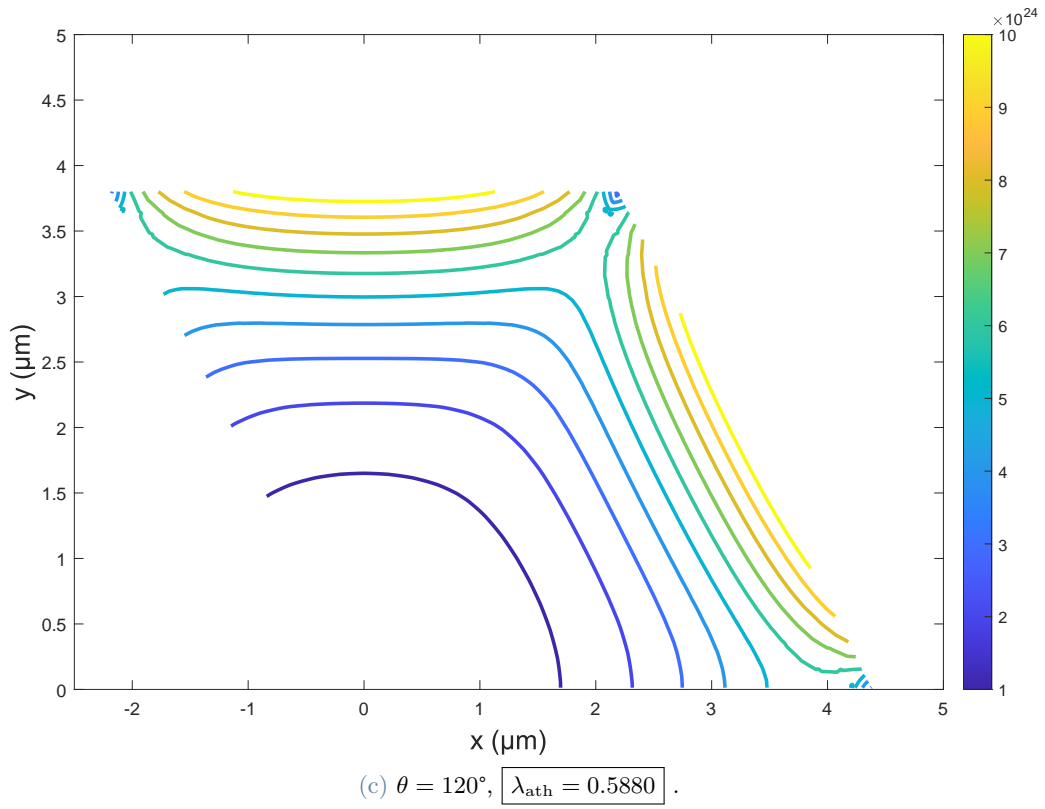


Figure 6: Comparison of the gas diffusion gradient shape with respect to the grain-edge inclination angle.

Aligned with this trend, it is anticipated that the value of λ_{ath} will be notably small for values close to $\theta = 90$ (6a), gradually increasing with higher values of θ . Eventually, as theta continues to increase, λ_{ath} is expected to approach a value close to unity (Figure 6d), indicating a significant transition in the behavior of gas diffusion. Indeed, it is apparent that, in coherence with the trend of the concentration gradient becoming more uniform for larger values of theta, and even resembling the gradient in a spherical grain, the athermal venting factor will tend to collapse to the value computed by Claisse and Van Uffelen. This alignment is consistent with their representation of the fuel grain as spherical in the diffusion process, as stated in Section 2.

Having elaborated on the two primary nuanced dependencies influencing athermal fission gas release, we can now briefly delve into the remaining factors affecting gas diffusion in the fuel grain and offer clarification on the respective ranges that were chosen in this study.

The motion of gas atoms in a 2-D representation of the fuel grain follows an inhomogeneous diffusion of the kind:

$$\frac{\partial c(x, y, t)}{\partial t} = \nabla \cdot \left(D \nabla c(x, y, t) \right) + S \quad (12)$$

where D ($\text{m}^2 \text{s}^{-1}$) is the gas diffusivity, x, y (m) are the spatial coordinate in Figure 4, t (s) is the time, c (at m^{-3}) is gas concentration and S (at $\text{m}^{-3} \text{s}^{-1}$) is the gas generation rate.

Expanding upon Equation 12, several dependencies emerge. First is the geometry, which hinges upon the dimensions of the grain, characterized by the length l of the rhombus edges. This value can be derived from an assumed equivalent grain radius a through geometrical conversion:

$$l = \frac{1}{3} D_{\text{TKD}} \quad (13)$$

where D_{TKD} (m) is the equivalent diameter of the TKD and it can be expressed as $D_{\text{TKD}} = 1.1(2a)$.

Second, the diffusion process is dictated by the gas diffusivity D and varies with time t and, equivalently with burnup β , parameter of our primary concern. Lastly, the diffusion of gas is influenced by the generation rate in irradiation cases, or alternatively, by the initial concentration in annealing scenarios. Intuitively the generation rate is directly proportional with respect to the fission rate.

These inter-dependencies underscore the multifaceted nature of gas diffusion within the fuel grain, necessitating a comprehensive approach in understanding and modeling its behavior. Nonetheless, navigating these dependencies and their intricate physical interconnections poses complex challenges. Furthermore, despite the precision achievable through the utilization of high-fidelity code, the computational cost associated with its implementation can prove burdensome and impractical for FPC applications. For these reasons, it was decided to lump all the information relating to the aforementioned dependencies, feeding into the computation of the factor λ_{ath} , into a surrogate model.

Several machine learning (ML) methods were explored, ranging from Support Vector Machines (SVM) to Robust Trees and Artificial Neural Networks (ANN). However, for the sake of simplicity and primarily for interpretability reasons [22], a feed-forward neural network (FNN) emerged as the optimal and most efficient choice. The architecture of the FNN is constructed featuring ten neurons and can be visualized in Figure 7.

The FNN was trained using a synthetic data-set generated from simulations of the previously mentioned high-fidelity code, comprising of 10348 observations with a seven-dimensional feature space, encompassing the aforementioned dependencies, described in Table 2.

The dataset was partitioned into training (70%), validation (15%), and test(15%) data according to a random sampling. The network’s training was optimized using the Levenberg–Marquardt algorithm, and its performance, outlined in Table 1, was assessed in terms of the mean square error (MSE).

Table 1: Performance of the neural network.

	Observations		MSE
Training	7244	70%	0.0038
Validation	1552	15%	0.0043
Test	1552	15%	0.0042

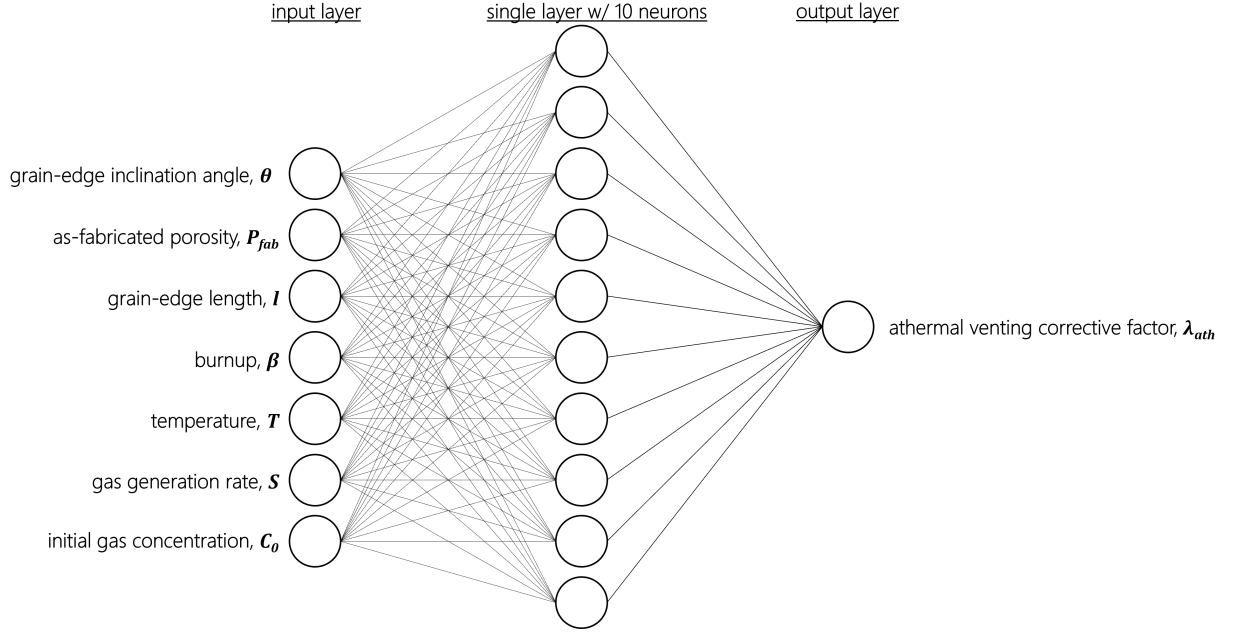


Figure 7: Schematic representation of the feed-forward neural network.

Table 2: Validity range of the features

Quantity	Definition	Range		Unit of Measurement
θ	Grain-edge inclination angle	90 - 135		$^{\circ}$
P_{fab}	As-fabricated porosity	2 - 9		%
l	Grain-edge length	3.67 - 11 ^a		μm
β	Burnup	0-50 ^b		$\text{MWd kg}_{\text{UO}_2}^{-1}$
T	Temperature	300-1600		K
S	Gas generation rate	Irradiation	Annealing	at $\text{m}^{-3} \text{s}^{-1}$
		$10^{18} - 10^{20}$	0	
C_0	Initial gas concentration	Irradiation	Annealing	at m^{-3}
		0	$10^{19} - 10^{24}$	

^a The range of values assigned to the TKD's edge length stems from a supposed range of equivalent spherical grain radius that spans from 5 to 15 μm .

^b This value represents a benchmark burnup level essential for evaluating high-burnup performance and assessing the applicability of our model. As this threshold is approached, the microstructure of the fuel is anticipated to undergo significant changes that necessitate a different modeling approach. Irradiation progressively alters the structure of the interconnected open porosity network. The percolated network of tunnels is altered and the formation of a novel porosity is observed in the fuel. This new structure is characterized by the presence of small, dense pores, particularly concentrated in the rim region of the fuel pellet [23].

The preceding discussions have established a framework for understanding the physics underlying athermal FGB. However, translating these predictions into a robust and reliable model necessitates a critical evaluation of its performance. In particular, the weight that the model proposed in this work holds must be pondered and assessed with respect to experimental data. This will be explored in more detail in Section 4.

3. Connected Phenomena

As referenced in Section 1, various other phenomena significantly influence fuel behavior in low-temperature applications and impact the evolution of open porosity. Among these phenomena are solid swelling and fuel densification, both of which are crucial to comprehensively understanding fuel behavior.

In this section, an examination of these two phenomena is proposed and models designed to effectively incorporate them into the SCIANTIX code are presented.

3.1. Fuel Solid Swelling

Swelling is defined, according to Olander [24], as the fractional increase in the volume of the solid with respect to the initial volume of the as-fabricated fuel, or by:

$$\left(\frac{\Delta V}{V}\right) = \frac{V - V^0}{V^0} \quad (14)$$

where V_0 is the volume of a region of fresh fuel and V is the volume of this same region after burnup β . These quantities can be visualised in Figure 8

Fuel swelling due to the replacement of heavy metal atoms by fission-product (FP) atoms is commonly considered as the sum of two contributions: one due to fission gases and a second one arising from all other fission products. On a general note, the former is treated separately because the inert gases xenon and krypton coalesce into bubbles within the fuel, whereas most of the remaining fission products are solids. However, it must be highlighted that at very low temperatures ($T < 1000^\circ\text{C}$), which align with the temperature range considered in this study, fission gases may not be sufficiently mobile within the fuel to form bubbles. In such cases, swelling due to these species is treated similarly to that resulting from other fission products. Since the system is assumed closed to solid fission products and fuel, none of these species is permitted to move into or out of the region during irradiation. According to these considerations Equation 14 can be rewritten as:

$$\left(\frac{\Delta V}{V}\right) = \left(\frac{\Delta V}{V}\right)_{\text{solid FP}} + \left(\frac{\Delta V}{V}\right)_{\text{gaseous FP}} \quad (15)$$

In turn, both single contributions can be expressed in a manner that resembles Equation 14. In particular, the solid fuel swelling term can be written as:

$$\left(\frac{\Delta V}{V}\right)_{\text{solid FP}} = \frac{V_s - V^0}{V^0} \quad (16)$$

Where V_s is the fuel solid volume after irradiation.

The physiochemical parameter that characterizes solid swelling is the partial volume of the fission products⁴, also referred to as covolume ($\frac{\text{cm}^3}{\text{atom}}$). This quantity represents the volume associated with each atom of fission products in their expected states in the irradiated fuel and it can be expressed as:

$$v_i = \frac{\text{volume}}{\text{atom of species } i} \quad (17)$$

Referring to Figure 8 we can write:

$$V^0 = v_U N_U^0 + v_{Pu} N_{Pu}^0 \quad (18)$$

Due to the similarity between UO_2 and PuO_2 , their respective covolumes can be assumed equal. Thus:

$$\begin{aligned} V^0 &= v_U (N_U^0 + N_{Pu}^0) \\ V_s &= v_U N_U + \sum_{i \in \text{solid FP}} v_i N_i \end{aligned} \quad (19)$$

⁴This volume includes the oxygen atoms associated with the fission products (if any).

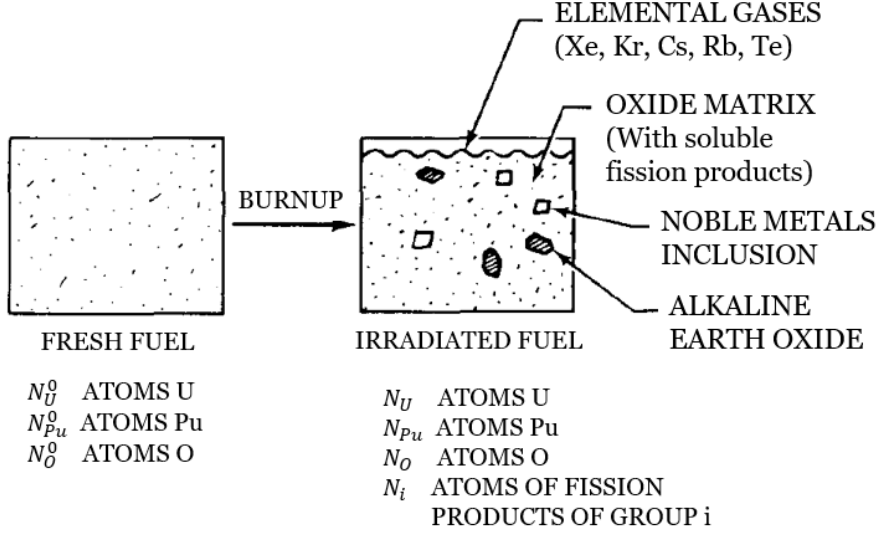


Figure 8: A unit volume of mixed-oxide fuel irradiated as a constant mass system [24].

Following Olander’s model and his treatment of concentration changes during burnup, and including it in Equation 16 will yield:

$$\left(\frac{\Delta V}{V}\right)_{\text{solid FP}} = \left[\sum_{i \in \text{solid FP}} \left(y_i \frac{v_i}{v_U} \right) - 1 \right] \beta \quad (20)$$

where y_i is the fission products yielding, reported in Table 3 along with the values of the specific volumes per each fission products group, and the burnup β is expressed in %FIMA.

	Covolume [$\frac{\text{cm}^3}{\text{atom}}$]	Chemical group	Elemental yield		
			U-235	Pu-239	15% Pu-239 85% U-238
Soluble fission products	40.93×10^{-24}	Zr + Nb	0.298	0.204	0.219
		Y + rare earths ^a	0.534	0.471	0.493
Alkaline earth oxide	71.2×10^{-24}	Ba + Sr	0.149	0.096	0.109
Metallic inclusions	14.73×10^{-24}	Mo	0.240	0.203	0.206
		Ru + Tc + Rh + Pd	0.263	0.516	0.456
Other fission products	31.1×10^{-24}	Cs + Rb	0.226	0.189	0.209
		I + Te	0.012	0.070	

a. La, Ce, Pr, Nd, Pm, Sm, Eu, and Gd.

Table 3: Fission product chemical groups and yielding

As mentioned before, at very low temperatures gaseous fission products Xe and Kr may not have enough mobility to coalesce into bubbles. For this reason, it was deemed appropriate to keep separate the contributions of solid fuel swelling due to the presence of Xenon and Krypton in intragranular solution. So, Equation 16 can be re-written as:

$$\left(\frac{\Delta V}{V}\right)_{\text{solid FP}} = \left[\sum_{i \in \text{solid FP}} \left(y_i \frac{v_i}{v_U} \right) - 1 \right] \beta + d[\text{Xe}]_{\text{sol}} + d[\text{Kr}]_{\text{sol}} \quad (21)$$

These two quantities are calculated in the SCIANTIX code from the fraction of the gas in the grain - retrieved from the solution of the spectral diffusion - that is at equilibrium.

Given these considerations, it is possible to include the contribution of solid swelling and account for its effect on the density update as follows:

$$\rho = \frac{\rho_{\text{solid}}}{1 - P} \quad (22)$$

where ρ is the fuel density, ρ_{solid} is the fuel solid density and P is the total porosity.

The solid density is the quantity that feels the effect of the solid swelling. This takes place in the measure that, as fission occurs and some fuel atoms are replaced by other fission products, the solid density, initially equivalent to the theoretical density, begins to diminish. This can be expressed as:

$$\rho_{\text{solid}} = \frac{\text{TD}}{1 + \left(\frac{\Delta V}{V}\right)_{\text{solid FP}}} \quad (23)$$

where TD is the theoretical density, equivalent to:

$$\text{TD} = \frac{\rho(t=0)}{1 - P_{\text{fab}}} \quad (24)$$

Regarding the evolution of porosity, it can be conceptualized as the simultaneous occurrence of three distinct mechanisms. These mechanisms can be considered independent of each other. Therefore, the overall porosity can be viewed as the combined effect of three factors: gaseous swelling, densification of as-fabricated porosity, and the evolution of porosity due to high-burnup structure⁵.

The former and latter contributions can be addressed respectively by employing models developed in [11, 25] and in [26, 27]. For what concerns the densification in the next section a dedicated semi-empirical model was developed.

3.2. Densification

As irradiation progresses and burnup increases, it is anticipated that the contribution of the as-fabricated open porosity will diminish. This reduction stems from in-pile densification, which leads to a decrease in total porosity and, consequently, a corresponding decrease in open porosity as well [7]. The experimental investigation conducted by Freshley et al. [28], underscored the primary factors influencing the densification process, including temperature, burnup, fission rate, as well as a combination of initial density, pore distribution, and grain size. Ideally, a comprehensive model capable of encompassing all these dependencies across a wide range of conditions would be desirable. Assman and Stehle [29] and Suk et al. [30] proposed four densification zones with different mechanisms for each. However, accurate values for the parameters involved are not always readily available. For this reason, multiple code developers [7, 31, 32] have implemented empirical expressions to characterize the fraction of original fabrication porosity that has annealed out as a consequence of densification, as a function of temperature, local burnup and grain radius. Of particular interest is the correlation employed in [32], where the annealed fraction, represented as f_{dens} , is computed as:

$$f_{\text{dens}} = \alpha[1 - \beta \exp(A_1 B) - (1 - \beta) \exp(A_2 B)] \quad (25)$$

where

$$\begin{cases} \alpha = \frac{1}{a[\mu\text{m}]} \exp\left(\frac{T-573}{620}\right) \\ \alpha\beta = 5.12 \exp\left(-\frac{5100}{T}\right) \\ A_2 = 1.5 \times 10^{-3} (\text{MWdkg}_{\text{UO}_2}^{-1})^{-1} \\ A_1 = 100A_2 \end{cases} \quad (26)$$

Van Uffelen [33] applied a modified version of Equation 25 for LWR fuels, such that the annealing out of porosity at high temperatures was increased. In his work the same formulation as proposed in [32] was kept, however, he altered the expression of the constant α , changing its value to: $\alpha = \frac{2}{a[\mu\text{m}]} \exp\left(\frac{T-773}{300}\right)$.

Employing an empirical methodology, however, entails sacrificing a deeper understanding of the underlying physics. Thus, in this study, we propose a semi-empirical approach to characterize fuel densification.

Initially, an examination of the dependencies was conducted, leading to the decision of setting aside the dependency on grain radius for several reasons. Firstly, simplicity and clarity in the formulation were prioritized. Since the influence of grain radius on densification remains uncertain, and our study employs normal grain-sized grains, the contribution of grain radius was disregarded [34]. Additionally, previous research (e.g. [35]) highlighted how limited or no grain growth is present during irradiation at low-temperature conditions, aligning with the scope of our study and further justifying this choice.

While maintaining dependencies on burnup and temperature, the primary idea was to model densification as a burnup-dependent process, influenced by a temperature-dependent source term described by the differential equation in Equation 27.

⁵This three effect can be treated in this manner only for the application we consider in this work. When HBS restructuring progresses, the contribution of the HBS porosity and the one concerning gaseous swelling cannot be thought of as linear separable anymore.

$$\frac{df_{\text{dens}}}{d\beta} = k_{\beta} f_{\text{dens}} + S(T) \quad (27)$$

where the source term $S(T)$ was modelled as exponential in nature.

$$S(T) = k_{T,1} \exp(k_{T,2} T) \quad (28)$$

The parameters k_{β} , $k_{T,1}$, and $k_{T,2}$ are constants to be determined through experimental data. In this work, the comprehensive study of UO_2 fuel densification performed by the Edison Electric Institute/Electric Power Research Institute (EEI/EPRI) [36] served as the cornerstone for this parameterization step, in agreement with the approach employed in the FUDENS model [37].

As a result, the values of the above-mentioned constants were found to be: $k_{\beta} = 2$, $k_{T,1} = 0.006$, and $k_{T,2} = 0.002$. The densification process of the fabrication porosity is an irreversible process, to ensure this, the densification factor was modelled as monotonically increasing with burnup:

$$f_{\text{dens}}(bu^f) = \max\{f_{\text{dens}}(bu^i), f_{\text{dens}}(bu^f)\} \quad (29)$$

where bu^i and bu^f are respectively the initial and final value of burnup.

The comparison between the results of the densification model proposed in Equation 27 and the experimental data from [36] can be visualised in Figure 9. The densification factor f_{dens} was then employed to update the fabrication porosity.

Complete elimination of porosity during densification is neither physically realistic nor aligned with experimental observations [38–40]. Therefore, the concept of residual porosity has been introduced. The fraction of porosity that persists within the fuel matrix after densification has occurred, and, on a general note, it deeply depends on the specific type of fuel employed. For the sake of simplicity in this study, a constant residual porosity value of 75% of the initial as-fabricated porosity was assumed. With this consideration, the influence of the densification factor on the updated porosity value can be incorporated using Equation 30.

$$P_{\text{fab}}^f = P_{\text{res}} + (P_{\text{fab}}^i - P_{\text{res}})(1 - f_{\text{dens}}) \quad (30)$$

where P_{fab}^f and P_{fab}^i are respectively the final and initial value of fabrication porosity and P_{res} is the residual porosity.

Having established the model for as-fabricated porosity evolution, we now turn our attention to open porosity densification. In contrast to the approach adopted by Van Uffelen [33], the fraction of original porosity and the fraction of open porosity that have annealed out during irradiation are not assumed to be equal. This assumption implies a linear relationship between the two quantities, which - as discussed before - might not fully capture the complex mechanisms governing the open pore structure. Consistent with the treatment of the relationship between P_{op} and P_{fab} , Equation 11 is employed to determine the updated open porosity value after each densification step as presented in Section 2.

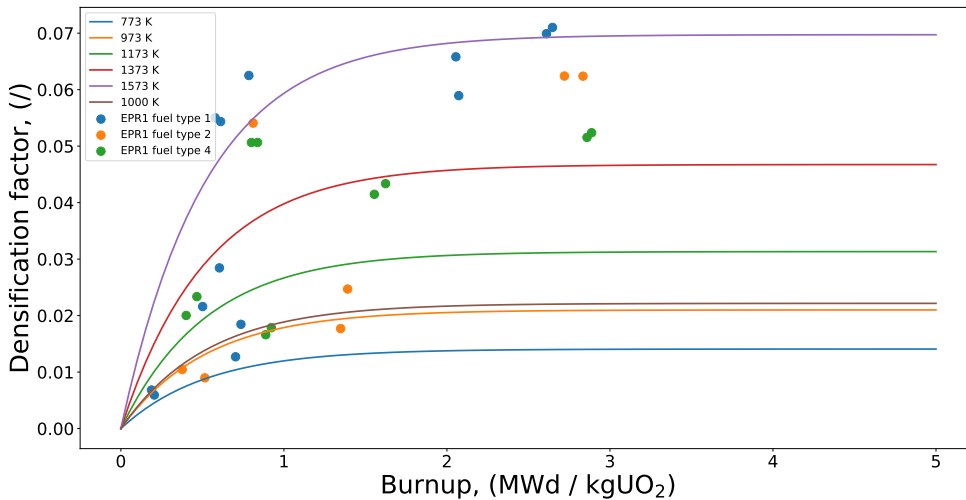


Figure 9: Densification of porosity with respect to the burnup, according to Equation 27 evaluated at different temperature levels, compared to experimental data [36].

4. Results

The consistency and predictive capabilities of the models developed in this work and integrated into the SCIANTIX code are tested using data available in the open literature. Specifically, a set of separate effect tests was conducted to assess the performance of SCIANTIX in standalone conditions, by employing the Kashibe [13] and Baker [14] experimental cases as benchmark scenarios. Additionally, to further explore the behavior of our AI-enhanced athermal fission gas release model across a broader range of temperatures and burnup values, a synthetic dataset was generated. This dataset was built considering the same fuel composition of the Baker tests and spanning a temperature range from 373 to 2073 K and irradiating until a final burnup level equal to 50 MWd/kgUO₂. The test cases employed in this study are mapped in Figure 10.

In the forthcoming section, we offer an overview of the experimental cases considered alongside the results obtained in this study.

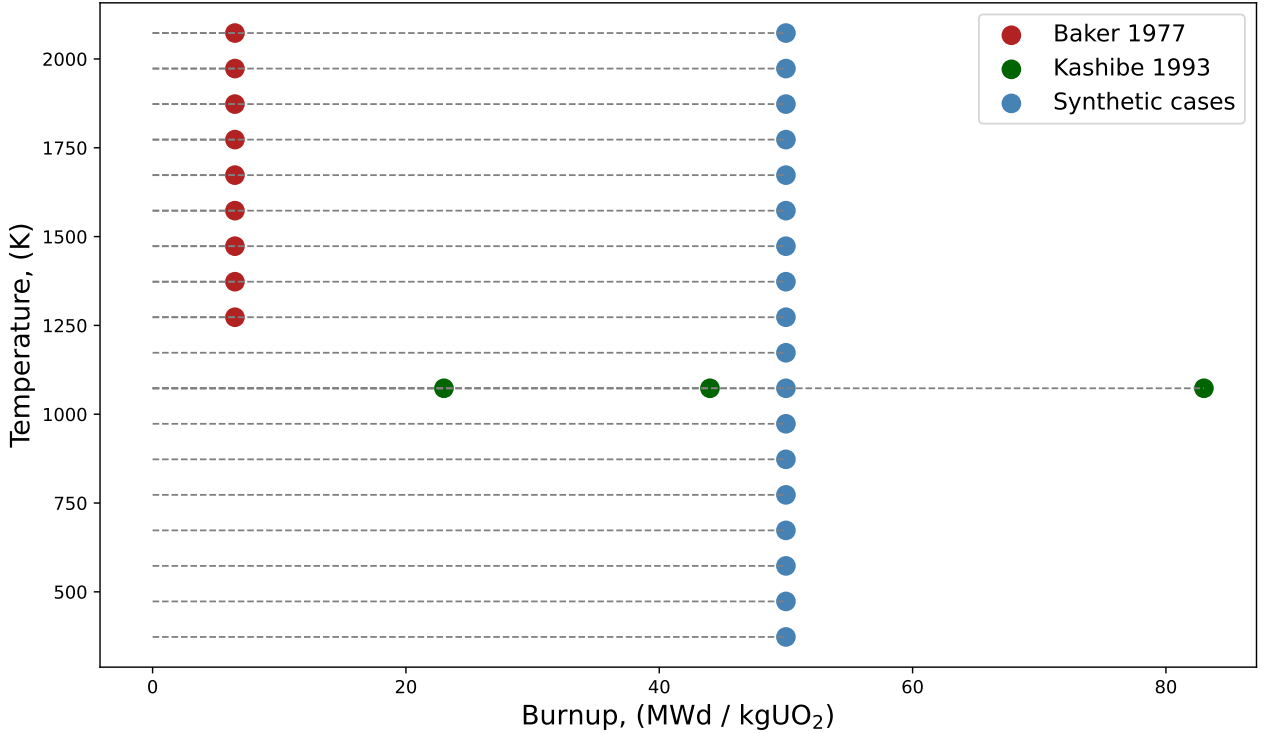


Figure 10: Experimental and synthetic cases employed in the separate effect tests of the AI-enhanced athermal fission gas release model developed in this work.

4.1. Kashibe Reference Case

The experimental campaign studied by Kashibe [13] reviewed the outcomes of a comprehensive PIE at Nippon Nuclear Fuel Development Co. [41, 42]. The primary objective was to elucidate the microstructural changes, with particular focus on intragranular bubble characteristics, in UO₂ fuels subjected to irradiation and subsequent out-of-pile annealing examined under Light Water Reactor (LWR) conditions. The specimens employed in the experiments were taken from UO₂ fuel pellets irradiated either to 6-44 GWd/t in a commercial Japanese Boiling Water Reactor (BWR) at Fukushima Daiichi Nuclear Power Station Unit No. 3, or to 83 GWd/t under pressurized water reactor (PWR) conditions in a the BR3 test reactor in Belgium. The latter fuel rod was part of the international High Burnup Effects Program (HBEP)[43]. Experienced maximum temperatures at the location of the specimens were estimated to be about 800°C from their maximum linear heat generation rates. Table 4 summarizes the specifics of the utilized fuel. Specifically, this analysis focuses on the base-irradiated experiments conducted at 23 and 44 GWd/t under BWR conditions, as well as at 83 GWd/t under PWR conditions. The latter case is of particular significance as it allows us to examine the behavior of our model under conditions that are beyond the range presented in Table 2, providing insights into its performance under stress conditions.

The Kashibe test cases play a crucial role as a benchmark for assessing the standalone performance of the AI-enhanced model of athermal fission gas release as well as the semi-empirical models for porosity densification

and solid swelling, integrated into the SCIANTIX code. Furthermore, a comparative analysis is conducted between our athermal FGR model and the approach developed by Claisse and Van Uffelen. Additionally, the performance of SCIANTIX in base irradiation cases, without an athermal release model, is also examined for comparison.

Table 4: Fuel pellet and rod design characteristics of the Kashibe test cases.

Fuel		BWR	PWR
Burnup	(GWd t ⁻¹)	6-44	83
Pellet density	(%TD)	95	93
²³⁵ U enrichment	(%)	1.5	7.0
Grain size	(μm)	9	13
Pellet diameter	(mm)	10.6	8.2
Pellet hole diameter	(mm)	-	2.5
Pellet-cladding gap	(mm)	0.23	0.17
He fill gas pressure	(MPa)	0.1	2.9
Active stack length	(mm)	3660	1017
Cladding material		Zircaloy-2	Zircaloy-4
Cladding outer diameter	(mm)	12.5	9.5

Examining Table 4, it becomes evident that the fuel employed under PWR conditions is characterized by a notable value of pellet density, equivalent, in turn, to a fabrication porosity value of 7%. This observation gains significance when considering Figure 3, where this value falls just above the transition region influenced by the anisotropic term in the relationship between open porosity and fabrication porosity. This prompts us to test our densification model using this specific case.

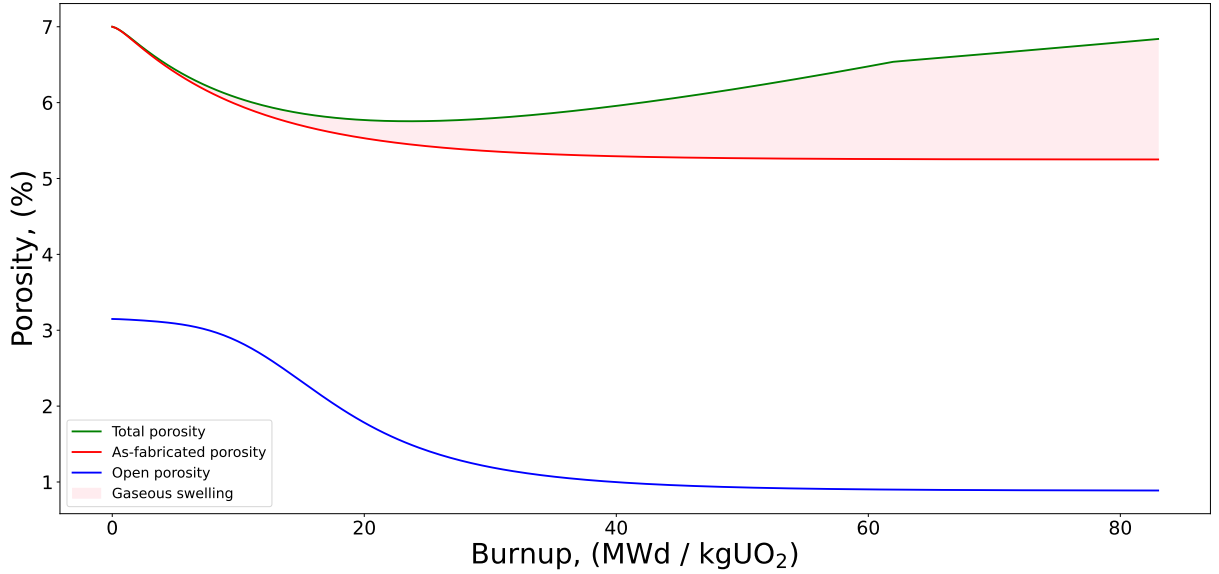


Figure 11: Evolution of the open porosity, alongside the fabrication and total porosity in the Kashibe test case, base-irradiated to 83 GWd/t under PWR conditions. The presence of anisotropy in the relationship between open porosity and as-fabricated porosity becomes evident right from the beginning of densification. As densification initiates from a high initial value of fabrication porosity, the transition region illustrated in Figure 3 is entered right from the onset of irradiation, and the open porosity exhibits the characteristic sigmoidal-shaped behavior associated with the anisotropic term, as seen in Equation 11.

Figure 11 depicts the temporal evolution, with respect to the burnup, of the three types of porosity: total porosity, as-fabricated porosity and open porosity. As irradiation progresses, the as-fabricated porosity undergoes densification following the ODE proposed in Equation 27, until reaching a residual porosity value where

densification ceases. The total porosity initially follows the as-fabrication porosity until gaseous swelling begins to dominate, causing the total porosity to depart significantly from the fabrication porosity evolution. Of particular interest is the evolution of the open porosity. Starting from a relatively high initial value of the as-fabricated porosity, the initial open porosity level is also notably high. Referring to Figure 3, it's evident that at the onset of densification, the open porosity immediately enters a transition region influenced by an anisotropic effect in the relationship between open porosity and fabrication porosity. This anisotropic effect, possibly driven by percolation phenomena, further impacts the evolution of open porosity during densification. Eventually, the open pore structure contracts until collapsing around 30 GWd/t, resulting in the stabilization of the open porosity value. Having discussed the effect of fuel densification and highlighted the complex nature of the dependency between open porosity and as-fabricated porosity, we can evaluate the performance of our model for solid swelling in the same test case. In Figure 12, we illustrate the progression of solid fuel swelling resulting from the displacement of heavy metal atoms by fission products, alongside total swelling and gaseous swelling. Notably, we also depict the gas concentration in intragranular solution, a parameter of particular significance in our proposed approach to treating solid swelling. According to Equation 21, at temperatures below 1000°C, fission gases may lack the mobility required to form bubbles within the fuel matrix. In such instances, swelling attributable to these gases is akin to that arising from other fission products. Subsequently, we emphasize how the trend of fuel solid swelling closely mirrors the evolution of gas concentration in intragranular solution.

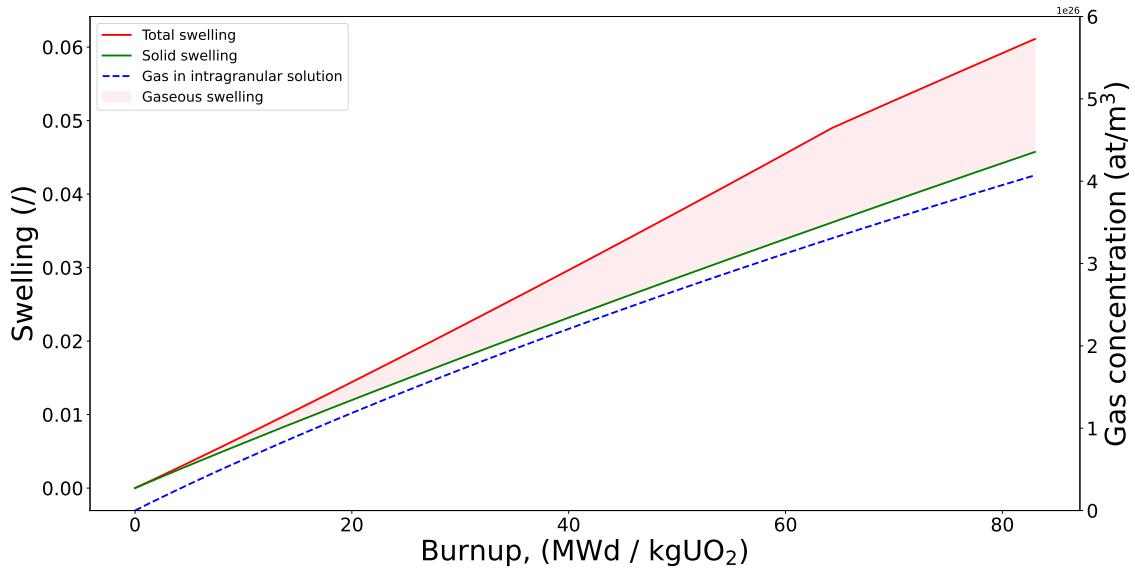
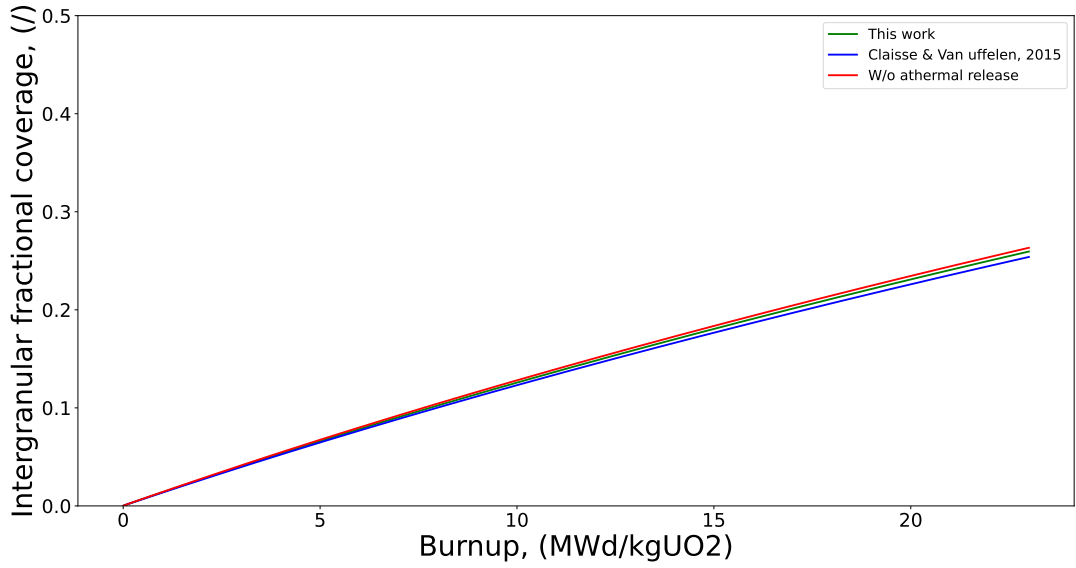
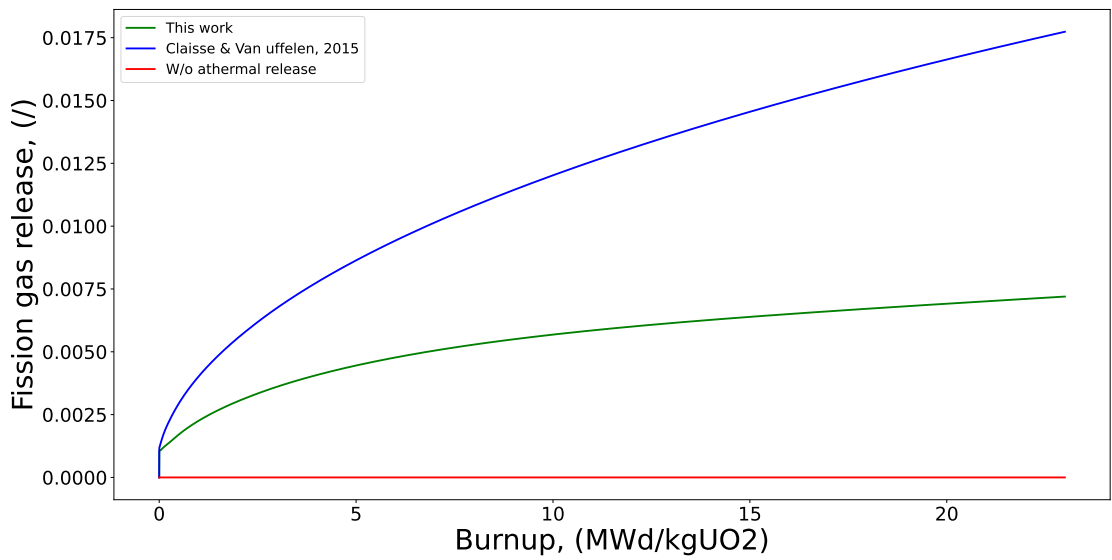


Figure 12: Evolution of fission product solid swelling, total swelling, and gaseous swelling, alongside gas concentration in intragranular solution in the Kashibe test case, base-irradiated to 83 GWd/t under PWR conditions.

Shifting our focus to the behavior of fission gas, we can evaluate how the model developed in this study compares to the previously described Claisse model and to the absence of an athermal release model altogether. With this scope, Figures 13, 14 and 15 depict the evolution of fission gas release alongside intergranular fractional coverage during the irradiation of the three Kashibe tests investigated: specifically, base-irradiated fuel up to 23 and 44 GWd/t under BWR conditions and up to 83 GWd/t under PWR conditions. The intergranular fractional coverage is a fundamental quantity in our analysis, as it strongly affects FGR. It can be roughly regarded as the fractional retention of fission gases at grain boundaries, therefore representing the proportion of the grain boundary area that is occupied by fission gas bubbles. As the intergranular bubbles grow and coalesce the intergranular fractional coverage increases until it reaches a saturation threshold. At that point, the fission gas release mechanism driven by thermal diffusion starts to dominate. It is assumed that, at this stage, the bubbles interconnect to form a percolated network across the grain boundary, and that a free path exists from interior grain boundaries to free surfaces of the pellet, as mentioned in Section 1. This could possibly occur through a network of tunnels that forms along the triple junctions in the grain structure [44]. Based on experimental observations of intergranular bubbles [11], a value of the intergranular saturation fractional coverage equal to 0.5 has been used for our simulations. In this study, the phenomenon of microcracking is not considered. Consequently, the mechanisms associated with the reduction and healing of saturation fractional coverage are not addressed, leading us to treat it as a constant parameter.

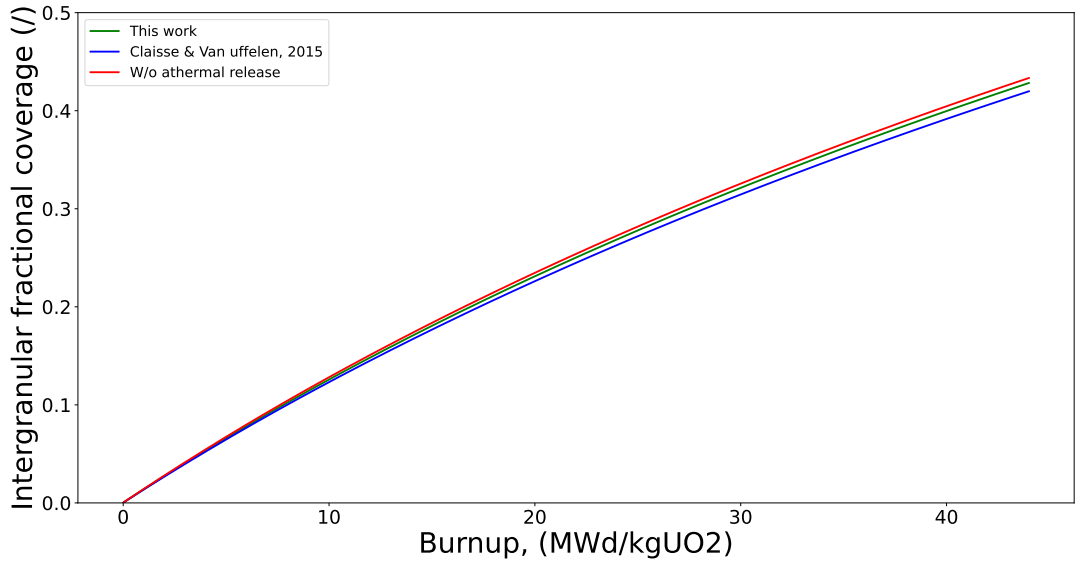


(a) Intergranular fractional coverage evolution in the Kashibe base-irradiated fuel to 23 GWd/t in a BWR.

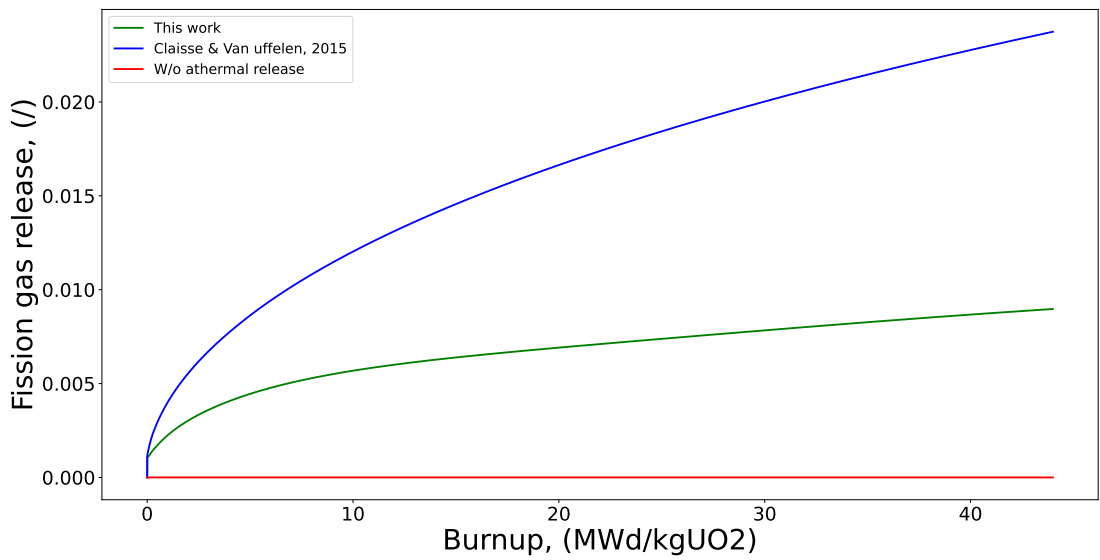


(b) Fission gas release evolution in the Kashibe base-irradiated fuel to 23 GWd/t in a BWR.

Figure 13: Athermal fission gas release, model comparison for the Kashibe base-irradiated fuel to 23 GWd/t under BWR conditions.

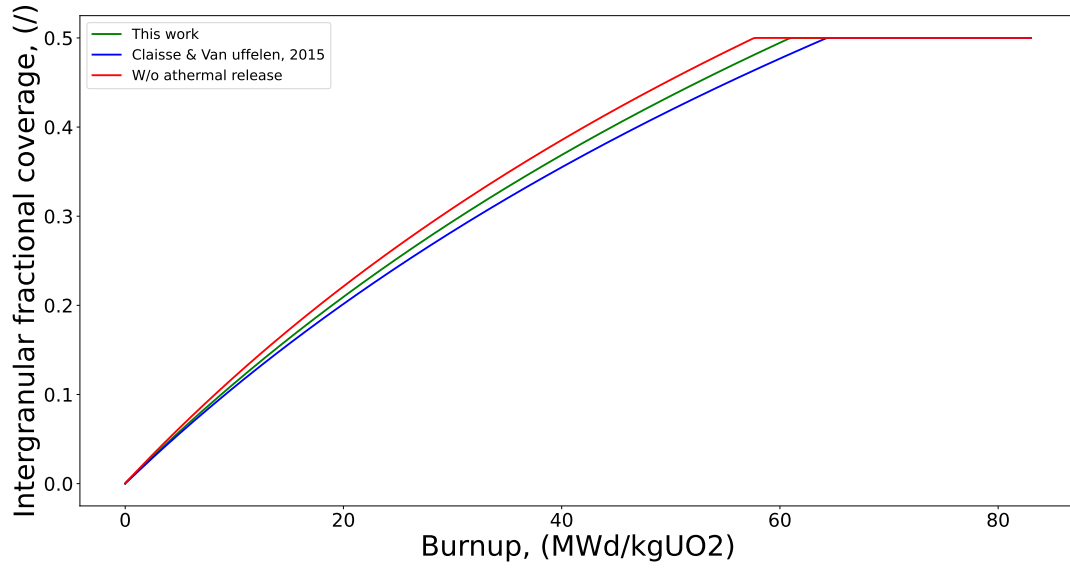


(a) Intergranular fractional coverage evolution in the Kashibe base-irradiated fuel to 44 GWd/t in a BWR.

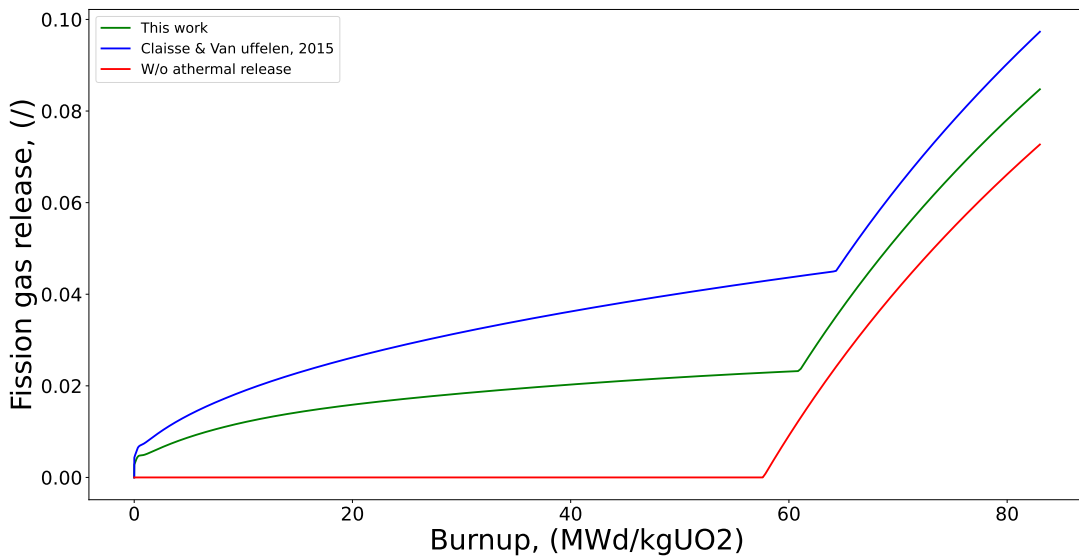


(b) Fission gas release evolution in the Kashibe base-irradiated fuel to 44 GWd/t in a BWR.

Figure 14: Athermal fission gas release, model comparison for the Kashibe base-irradiated fuel to 44 GWd/t under BWR conditions.



(a) Intergranular fractional coverage evolution in the Kashibe base-irradiated fuel to 83 GWd/t in a PWR.



(b) Fission gas release evolution in the Kashibe base-irradiated fuel to 83 GWd/t in a PWR.

Figure 15: Athermal fission gas release, model comparison for the Kashibe base-irradiated fuel to 83 GWd/t under PWR conditions.

Analyzing Figures 13a, 14a, and 15a, it is evident that all three models agree on the fact that the grain boundaries reach saturation in the PWR test case, while this is not achieved in the BWR test cases. Although there's slight variation in the evolution of intergranular fractional coverage, this effect is relatively weak. An interesting observation, as depicted in Figure 15a, is the variability in the burnup value at which saturation occurs when employing different models. Notably, the model lacking athermal release reaches saturation first, followed by the prediction of this study, and then by the Claisse model. This discrepancy in the predicted burnup values, marking the onset of grain boundary saturation, holds significance. It's worth recalling that SCIENTIX has been developed as a 0-D code, thus operating at a local level. While the integral behavior of the fuel may not strongly feel the impact of this effect, at a local level it could carry importance for assessing the regions within the fuel pellet where grain boundaries reach saturation.

A significant note can be made regarding Figures 13b, 14b, and 15b, where the three models exhibit distinct behaviors regarding expected fission gas release. Focusing on the BWR test cases, it is notable that the model without an athermal fission gas behavior predicts zero release. This discrepancy with experimental observations of fission gas release in base-irradiated scenarios underscores the importance of incorporating a model for athermal fission gas release.

Comparing the state-of-the-art model developed by Claisse and Van Uffelen with the one proposed in this study reveals a somewhat significant difference. While the Claisse model considers athermal fission gas behavior, its predictions estimate a fission gas release of around 1.75% for the case irradiated up to 23 GWd/t and almost 2.5% for the one irradiated up to 44 GWd/t. Moreover, according to the results of this model, FGR is expected to exceed 1% already at the beginning of the fuel life (for a burnup value around 6-7 MWd/kg). In contrast, our model predicts releases well below the 1% threshold, which is more consistent with experimental data.

Regarding the base-irradiation case at 83 GWd/t under PWR conditions, in agreement with our previous observations, saturation becomes evident. Notably, we reaffirm that the incubation time – defined as the time required for the grain boundaries to reach saturation – extends with the increase of athermal release. This phenomenon can be explained by the presence of an escape route for gas, provided by the open porosity. Consequently, the saturation of grain boundaries occurs later, thereby postponing the initiation of thermal diffusion in proportion to the extent of athermal release.

In contrast to the scenarios observed in the two BWR cases, it is anticipated that fission gas release in this base-irradiation reaches notably higher levels across all three models. While the final release may vary slightly among the three models, it remains within the same order of magnitude. This arises from the dominance of thermal diffusion once saturation is reached, rendering the effect of athermal release marginal. The heightened release can be attributed to inherent specifics in the composition of the fuel utilized for this specific test, alongside the significantly longer irradiation time. As detailed in Table 4, it is evident that the enrichment level is substantially higher here, standing at 7% as opposed to 1.5% in the BWR cases. Furthermore, as noted before, the initial fabrication porosity is characterized by a notably high value, indicating a correspondingly higher release in the athermal region. This highlights the relevance of the physical dependencies influencing athermal release, as presented in Section 2.2.

4.2. Baker Reference Case

The experimental study proposed by Baker aimed at describing an examination of the fission gas bubble distribution in uranium dioxide from experimental Steam Generating Heavy Water Reactor (SGHWR) fuel pins irradiated in the UKAEA's Winfrith SGHWR to $\approx 1\%$ burn-up at temperatures $< 2300^\circ\text{C}$ and at ratings of 25-46 watt/gram. The fuel pins examined were taken from experimental SGHWR clusters. The uranium dioxide pellets in the pins were 14.3 or 14.5 mm in diameter, 1.5 mm long with both ends dished to a depth of 0.4 mm and with a density of $\approx 97\%$ theoretical. An average ^{235}U enrichment equal to 2% was assumed. The experimental temperatures were estimated to have values between 1000 and 1800°C.

The entirety of the Baker dataset will be explored in the upcoming section. For now, let us focus on the coldest test case to further assess the behaviour of all three of the models developed in this work.

Beginning with the densification model, the evolution of porosity, as depicted in Figure 16, illustrates a trend akin to that observed in Figure 11: with ongoing irradiation, the initially fabricated porosity undergoes densification according to the ordinary differential equation proposed in Equation 27. This process continues until a residual porosity value is reached, signaling the cessation of densification. What is intriguing, however, is the fact that, while in the Kashibe test case at 83 GWd/t, the predominant effect of the relationship between fabrication porosity and open porosity seemed to be the one anisotropic in nature, in the current scenario, we can discern and appreciate the influence of the linear term in Equation 11. As densification advances, the open porosity, depicted here with an exaggerated factor of 10 for enhanced visual clarity, closely mirrors the evolution of the as-fabricated porosity.

Regarding the solid swelling model, it is worth reiterating that fuel solid swelling closely tracks the evolution of gas concentration in the intragranular solution, while total swelling ultimately reflects gaseous swelling. In

Figure 17, where the data is presented on a logarithmic scale, unlike Figure 12, the evolution of intragranular gas swelling is depicted, alongside corresponding experimental data for precision and validation. Finally, regarding the behavior of athermal fission gas compared to the Claisse model and the predictive abilities of SCIANTIX without an athermal FGR model, similar conclusions drawn from the analysis of the Kashibe test cases apply.

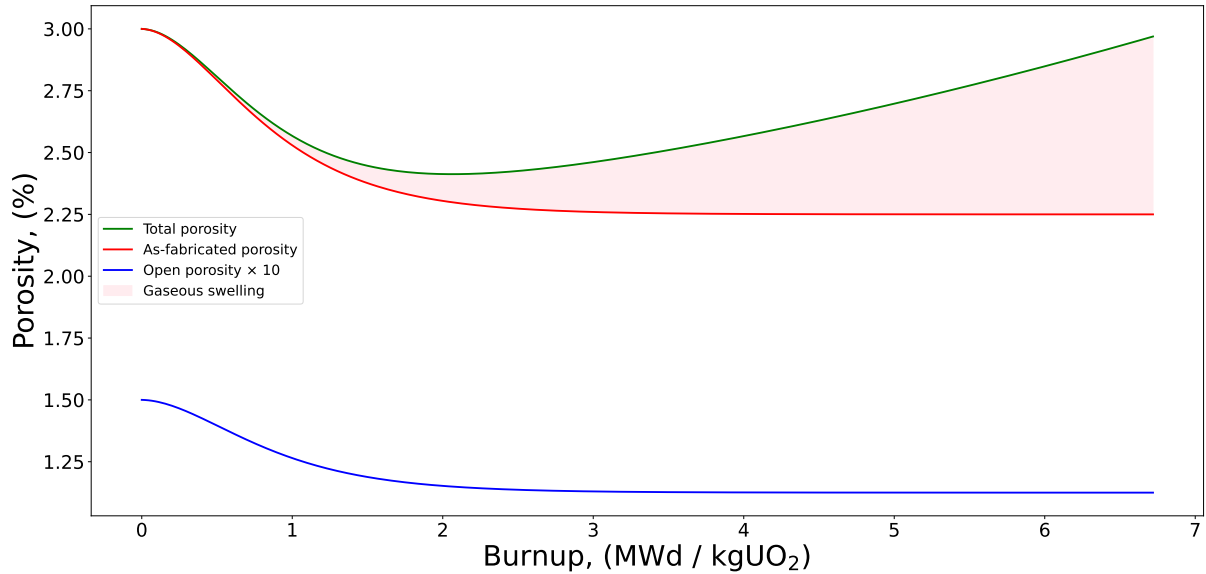


Figure 16: Evolution of the open porosity, alongside the fabrication and total porosity in the Baker test case at 1275 K. For the sake of visibility, the values of the open porosity have been enlarged by a factor of 10. It can be observed that the open porosity mirrors the trend of the fabrication porosity, drawing attention to the isotropic term of Equation 11.

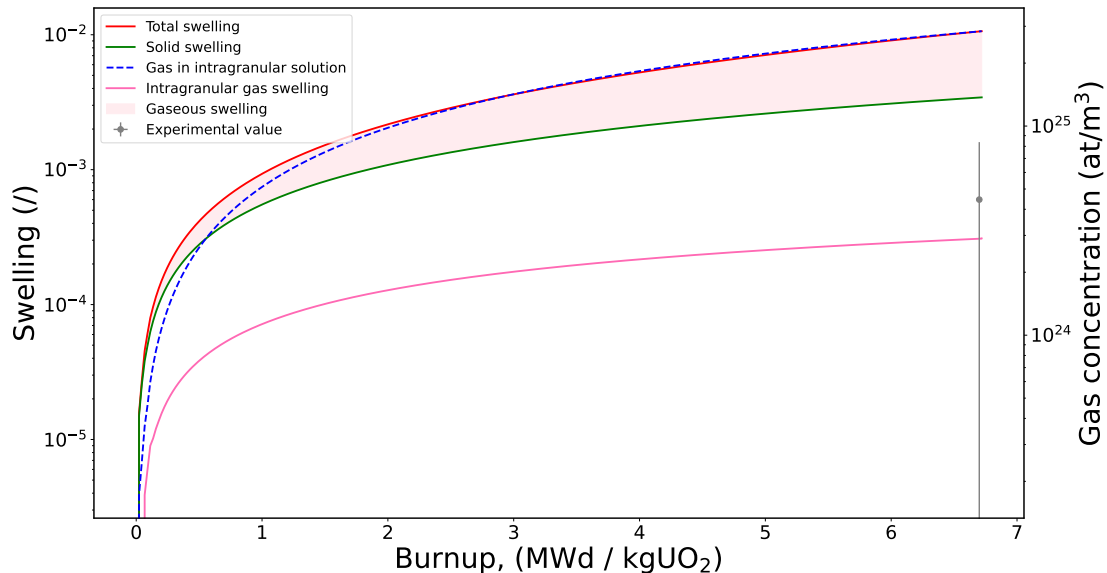
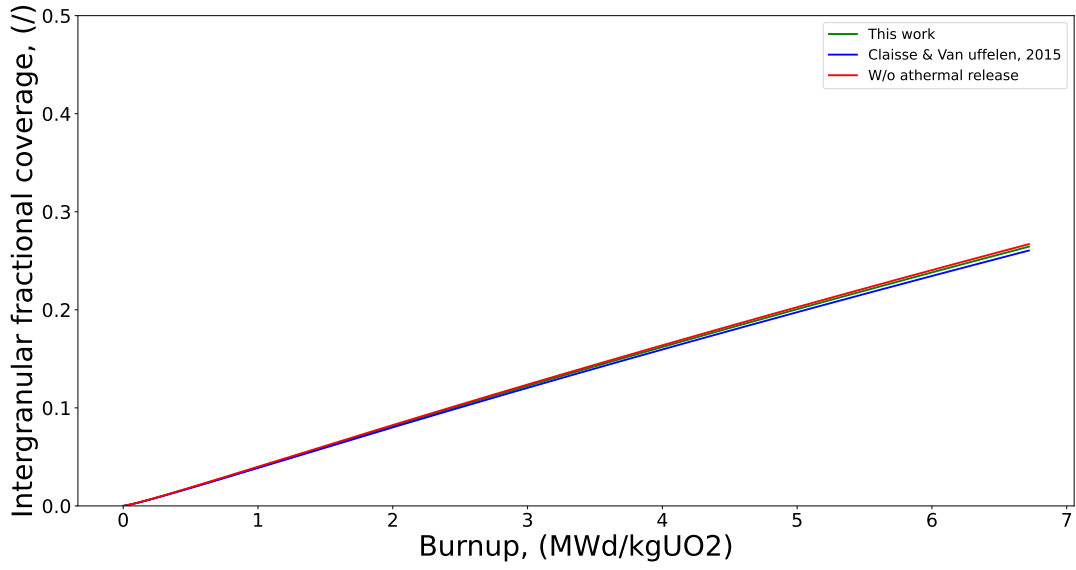
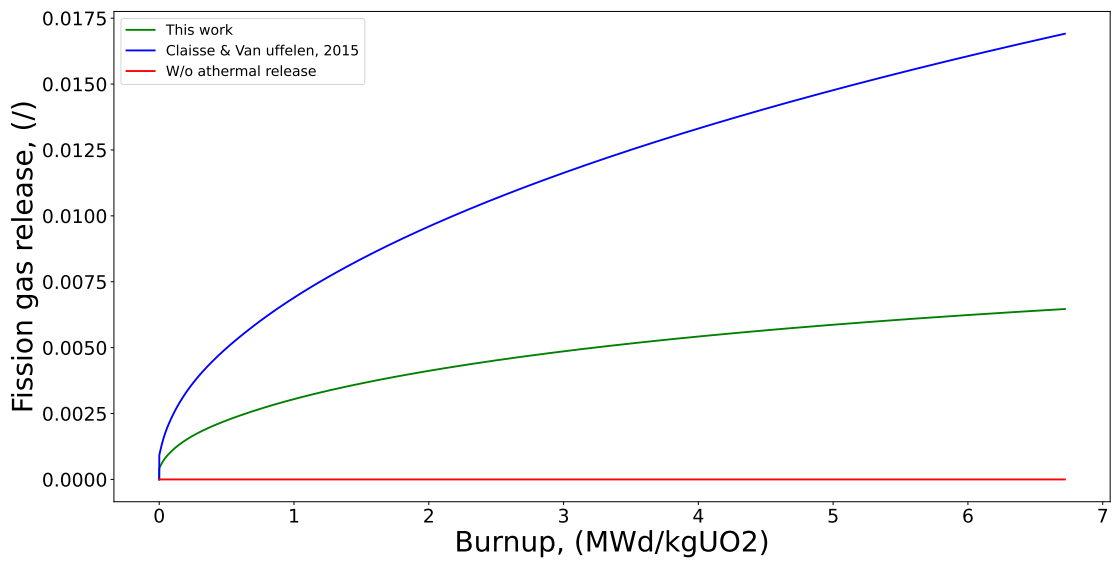


Figure 17: Evolution of fission product solid swelling, total swelling, and gaseous swelling, alongside gas concentration in intragranular solution in Baker test case at 1275 K. The plot is presented in logarithmic scale for the sake of visibility of the intragranular gaseous swelling and its corresponding experimental value.



(a) Intergranular fractional coverage evolution in the Baker base-irradiated fuel at 1273 K.



(b) Fission gas release evolution in the Baker base-irradiated fuel at 1273 K.

Figure 18: Athermal fission gas release, model comparison for the Baker test case at 1273 K.

4.3. Overall behaviour

Having acknowledged the potential of the athermal fission gas release model developed within this study, our attention is now turned towards investigating its behavior across a broader spectrum of separate effect test cases. This comprehensive evaluation encompasses not only the Baker and Kashibe cases but also a collection of synthetic cases, as mentioned earlier in this section. Moving forward, we propose a more in-depth analysis of the evolution of fission gas release, accompanied by a depiction of the trend in intergranular fractional coverage. For the sake of clarity in our presentation, the results pertaining to the histories of fission gas release are always truncated upon reaching saturation. This allows for a focused examination of athermal fission gas release exclusively, given that once saturation is attained, release driven by thermal diffusion dominates.

The following results are expressed in terms of a unique unit: the square root of burnup. We adopt this metric as it aligns with the nature of FGR diffusion, as described by the Boot model. Moreover, employing the square root of burnup provides a suitable approximation for short timescales, which are of particular interest in scenarios involving low irradiation, relevant to our study. According to this approximation, the FGR can be seen as directly proportional to the irradiation time. As we will observe in the following analysis, the behavior of fission gas release demonstrates a predominantly linear trend. This is indicative of a clear purely diffusive mechanism, which aligns with our description in Section 2.

At this point, let us evaluate the performance of our model across varying temperatures and at low burnup according to the Baker test cases. In Figure 19a a distinct trend emerges where the incubation time displays an inverse relationship with temperature. Specifically, as temperature rises, the time needed to achieve saturation decreases. Additionally, we observe that the behavior of the intergranular fractional coverage is non-linear. This is evident in the varying steepness with which saturation is attained as temperature increases, as well as in the fact that the distance between each case is not uniformly distributed across the temperature range. Such observations suggest the presence of mixed effects, implying that factors beyond temperature influence the incubation process. Notably, in certain experimental scenarios, saturation is not reached altogether.

Regarding the FGR, as depicted in Figure 19b, it's notable once again that the curves are truncated at the onset of saturation, as indicated in the corresponding graph of intergranular fractional coverage above. The trajectory of the curves exhibits a general similarity across all cases, albeit with subtle variations. Certain curves, such as the one corresponding to 2073 K, appear nearly horizontal, primarily due to truncation at saturation. Particularly, the behavior concerning temperature is not monotonic. An unexpected effect of temperature emerges, which is not easily predictable. Particularly noteworthy is the peak in release observed around 1700-1800 K, followed by a subsequent decrease. This phenomenon can be attributed to the mixed behavior of intragranular bubbles. As a consequence, the expected amount of athermal release at the beginning of life does not strictly follow a linear trend with temperature but rather depends on the intricate physics governing processes within the grain.

Another noteworthy observation is the presence of an initial peak in FGR at the incipit of irradiation. This peak arises from the fact that fuel densification requires a certain amount of time to initiate. At the beginning of irradiation, all the open porosity is readily available for fission gas to find an easy escape path to the rod free-volume. In this phase, the release exhibits a monotonically increasing trend, reflecting the pure diffusion occurring at the grain level. As time progresses, densification gradually affects the amount of available open porosity, which diminishes, leading to a decrease in FGR. Although fission gas production continues, the release is attenuated due to the shrinking network of open porosity. The fraction of open porosity that is annealed out is influenced by temperature, as elucidated in Section 3. Consequently, in this phase, the effects of temperature on fission gas release and densification intertwine, making it challenging to determine precise upper and lower bounds for the initial peak in terms of which temperature values result in more or less release at the earlier stages of irradiation.

Despite the range in temperature, for equivalent burnup levels, the fission gas release values ultimately exhibit a similar order of magnitude, with minimal variations. Thus, although there is indeed a certain dependence on temperature, it is not as pronounced as that observed at higher release rates. This further solidifies the concept of athermal behavior. It is interesting to note that, strengthened by these observations, we can essentially establish an upper bound for release based on temperature over a wide range of temperatures; a finding that carries significant engineering implications.

Now, we delve into the performance of our model in low-temperature scenarios across extended burnup levels, focusing on the Kashibe test cases.

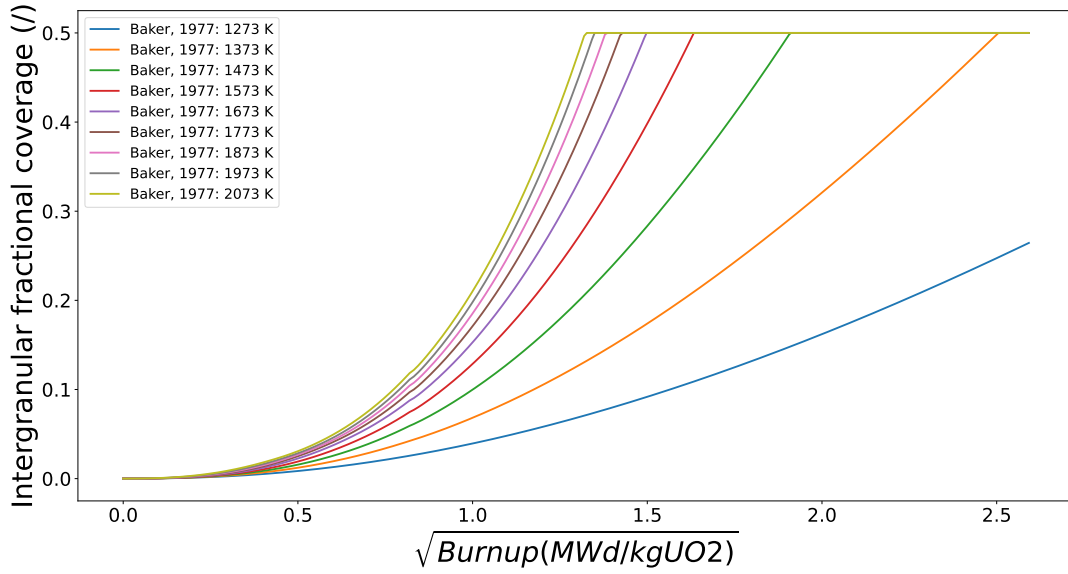
As previously discussed, it is confirmed that, at very low temperatures, saturation of grain boundaries is seldom reached, except at exceptionally high burnup levels. Similar to the Baker test case discussed earlier, the impact of porosity densification is visible at lower irradiation times, albeit somewhat less pronounced in the BWR cases. The predominant trajectory of the curves remains roughly linear, once again indicating a primarily diffusive phenomenon. However, as burnup increases, this trend gradually diminishes. This effect is particularly noticeable in the PWR test case. This can be attributed to the short irradiation time approximation becoming

invalid, as diffusion alone cannot fully explain the behavior of fission gas.

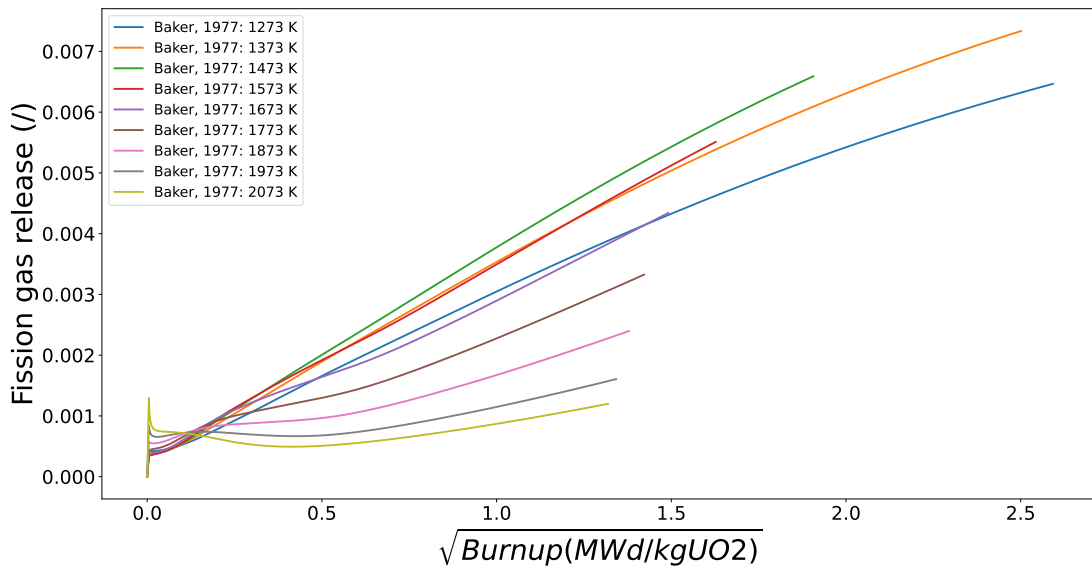
As mentioned previously, the fuel specimens subjected to base irradiation under BWR conditions demonstrate a low level of fission gas release, well below the 1% threshold. However, the test case irradiated under PWR conditions exhibits a significantly higher release from the outset of irradiation. Once again, this disparity can be attributed to the specific fuel composition of the HBEP sample utilized. Nonetheless, it is apparent that a bound for fission gas release can also be established in this case.

The experimental cases studied by Baker and Kashibe have shed light on crucial aspects of athermal fission gas release under various conditions. However, their studies only partially cover the spectrum of temperatures and burnup levels that we seek to explore. To bridge this gap, additional synthetic cases were introduced to our dataset, as depicted in Figure 10. It is important to note that our focus was solely on base-irradiation scenarios, and thus transient analyses were not within the scope of this study. These synthetic cases were crafted on the base of the Baker cases and utilizing the same fuel specifications, irradiating up to a target burnup of 50 GWd/t, spanning a temperature range from 373 to 2073 K.

In Figure 20 the results of these synthetic simulation is presented. The observations that can be drawn from them mirror what has already been discussed for the Kashibe and Baker cases. This underscores the fact that, although the fission gas release trend manifests some non-linearity, the model does not present regions of unpredictability and is consistent over the whole range of our map.

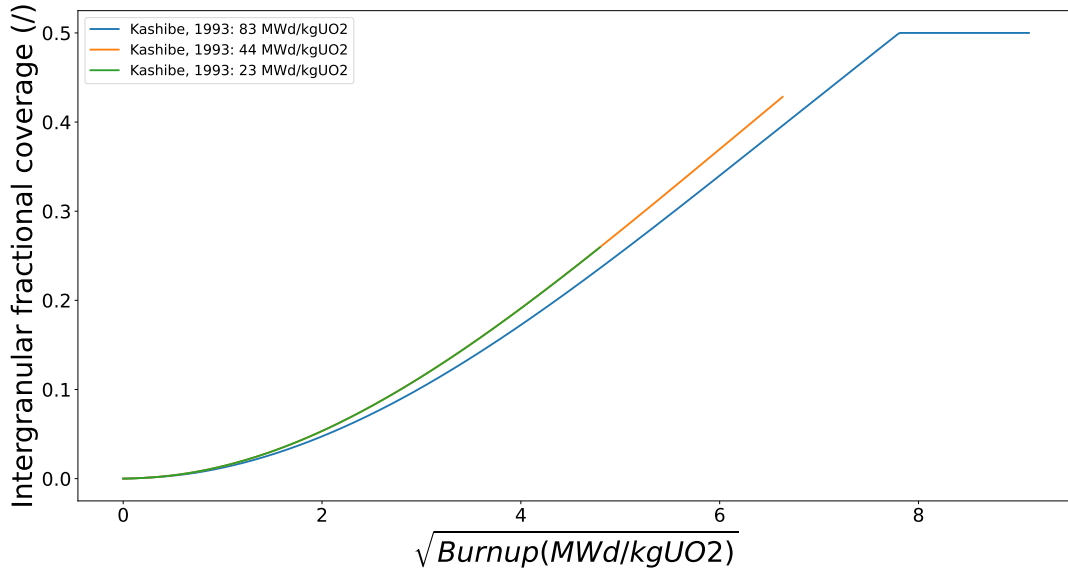


(a) Intergranular fractional coverage, Baker cases evaluated across the entirety of their temperature range from 1273 to 2073 K

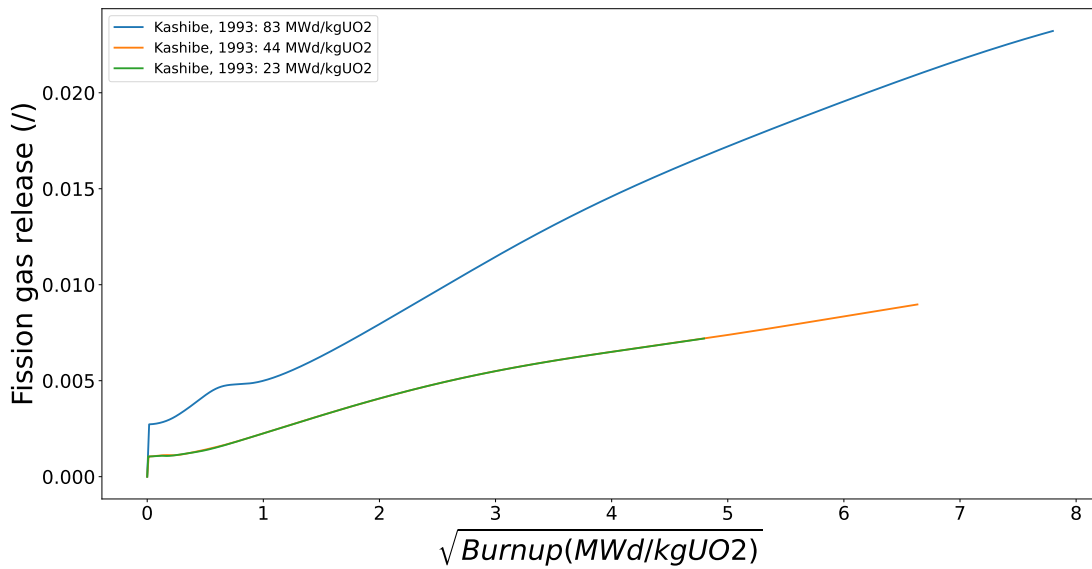


(b) Fission gas release, truncated at the onset of saturation, Baker cases evaluated across the entirety of their temperature range from 1273 to 2073 K

Figure 19: Separate effect test on the AI-enhanced model developed in this work applied to the Baker (1977)[14] cases.

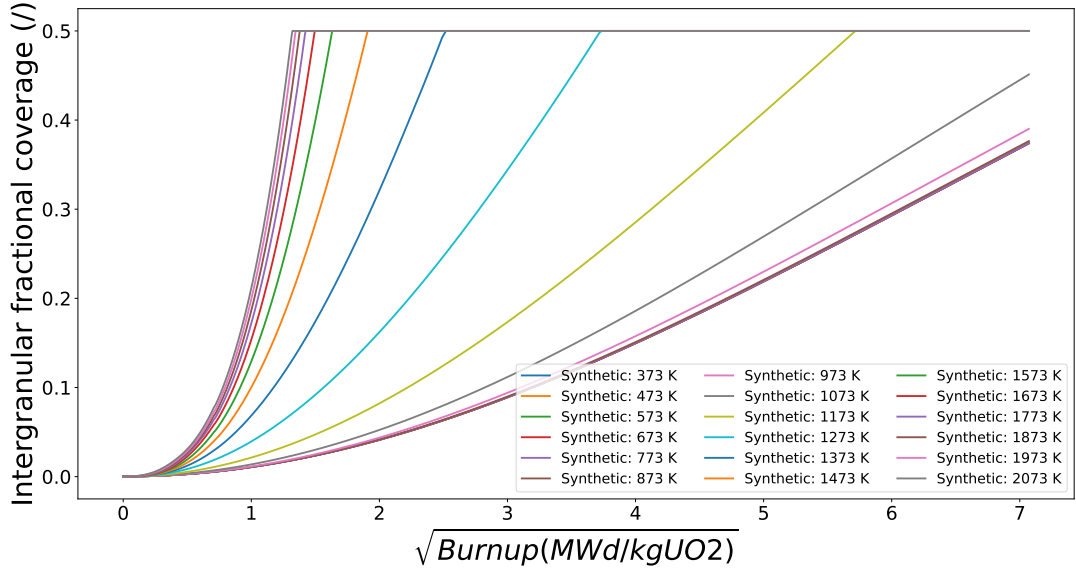


(a) Intergranular fractional coverage, Kashibe cases evaluated across the entirety of their burnup range from 23 to 83 GWd/t

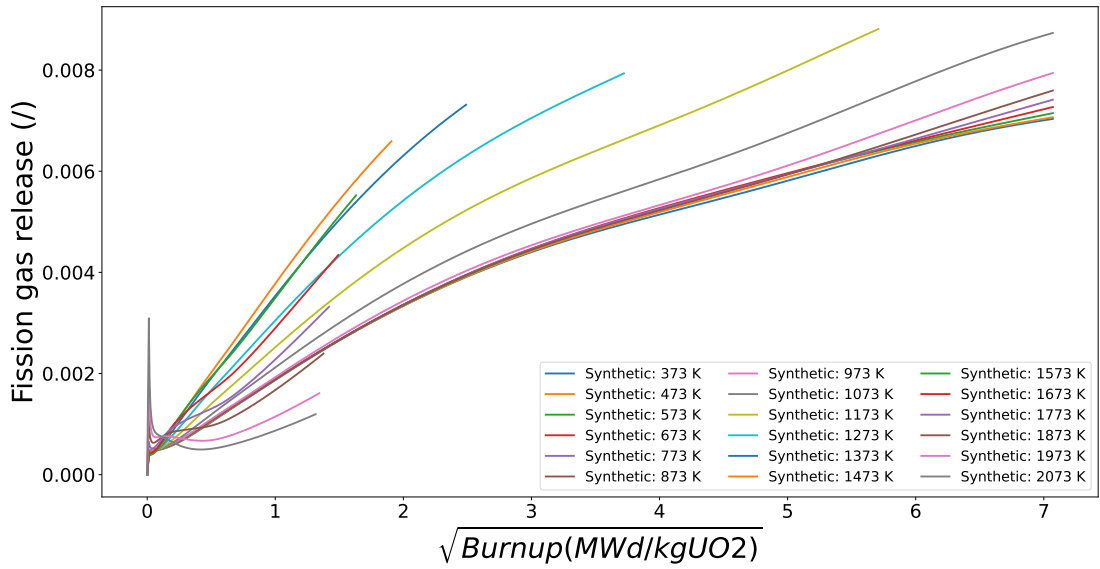


(b) Fission gas release, truncated at the onset of saturation, Kashibe cases evaluated across the entirety of their burnup range from 23 to 83 GWd/t

Figure 19: Separate effect test on the AI-enhanced model developed in this work applied to the Kashibe (1993)[13] cases.



(c) Intergranular fractional coverage, synthetic cases evaluated across the entirety of their temperature range from 373 to 2073 K.



(d) Fission gas release, truncated at the onset of saturation, synthetic cases evaluated across the entirety of their temperature range from 373 to 2073 K.

Figure 20: Separate effect test on the AI-enhanced model developed in this work applied to synthetic cases.

5. Discussion

Having studied in detail the behaviour of the AI-enhance model for athermal fission gas release developed in this study across a wide spectrum of temperatures and burnup levels, we now turn our attention to the significance of our model for experimental cases utilized in validating the SCIANTIX code.

From our earlier discussion, it became evident that the behavior of athermal fission gas behaviour plays a crucial role in assessing fission gas release in low-temperature conditions. Its significance persists until saturation of grain boundaries is reached, beyond which its impact diminishes. Once the onset of thermal diffusion is reached, its importance becomes minor. Thus, our objective is to determine the temperature and burnup levels at which this saturation occurs for each of the studied cases. Subsequently, we will compare these findings with experimental cases, where saturation is anticipated not to occur due to the minimal experimental release of fission gas, typically, at most, in the order of 1-2%. As briefly mentioned in Section 1, the experimental data on fission gas release from base irradiation cases include AN3 [15], REGATE, HATAC-C2 [16], and CONTACT1 [17]. Each case was evaluated at its respective average fuel temperature. Their specifications are summarized in Table 5. Additionally, we aim to explore and map the temperature and burnup thresholds at which fission gas release reaches 1%, and to extend our comparison to include the Vitanza threshold [45, 46] alongside the already mentioned experimental data points.

In this section, we will offer an overview of these experimental cases and conduct a detailed analysis of how our model performs in comparison to them.

The Risø-3 is a bump-test program aimed at investigating FGR and microstructural changes of several refabricated and reinstrumented fuel rods. Within the Third Risø Project, seven transient tests were carried out on an experimental UO_2 fuel supplied by the Advanced Nuclear Fuel Company (ANF, now Siemens Nuclear Power Corporation). The ANF fuel was base-irradiated in the Biblis-A reactor in Germany. The irradiation spanned four reactor cycles beginning on July 10th, 1982 and ending on October 3rd, 1985. At the end of this period, the pin average burnup was 4.3 to 4.4% FIMA, equivalent to approximately $35.6 \text{ MWd kg}_{\text{UO}_2}^{-1}$. The highest linear power seen by the fuel ranged from 24.1 to 26.7 kW m^{-1} . Powers of this magnitude were recorded at the beginning of the second and fourth reactor cycles. Fission gas release in the base irradiation was very low; only 0.2-0.3% release was measured when four pins were punctured. While rods from Risø-3 program have been extensively analyzed and employed to validate several FPCs, e.g., the BISON code [47], the COSMOS code [48, 49], and also separate FGB models [50–52], we reiterate that this study aims to enhance the predictive capabilities of SCIANTIX in base irradiation cases. Consequently, our focus in this section will be on evaluating the base irradiation, particularly of test AN3.

The REGATE experiment belongs to the Fuel Modeling at Extended Burnup (FUMEX-II) program [16] and to the IFPE database. A short fuel segment irradiated in a commercial PWR and ramped in the SILOE test reactor was employed for this test case. The original segment was irradiated in the ravlines 5 PWR up to 47.415 $\text{MWd/kg}_{\text{HM}}$. Nondestructive post-irradiation examination (PIE) was conducted on discharge with measurements made on clad diameter and a FGR of 1.5% estimated by non-destructive ^{85}Kr gamma measurement.

The HATAC project is part of the IAEA FUMEX-II benchmark. This experiment involved irradiating two fuel segments from pre-irradiated 17×17 PWR fuel rods in the SILOE test reactor. In this analysis, we focus on the HATAC C2 case due to the availability of higher-quality experimental data and its more relevant burnup range. The HATAC C2 fuel rod underwent initial irradiation at the Fessenheim-1 Nuclear Power Plant up to an average burn-up of 45.79 MWd/kgU , followed by re-irradiation in the SILOE reactor. During re-irradiation, a series of short power transients were conducted, with linear heat rates ranging between 18-20 and 28-29 kW/m . Power holding periods lasted approximately three hours, with a ramp rate of about 5 kW/m/min . A gas sweeping device was used to measure the release kinetics of both stable and radioactive fission gas during these transients.

The CONTACT1 experiment took place in the SILOE reactor, in which short fuel rods with five UO_2 pellets (for a total length of 7 cm) with a Zr-4 cladding was irradiated up to burnup values of about 22 MWd/kgU . The rodlet was located in a PWR loop, at 13 MPa, with a cladding temperature of 330°C from the nucleate boiling regime. The Linear Heat Rate (LHR) (of about 40 kW m^{-1}) was measured by rhodium neutron detectors with an accuracy on the measurement of 3%. The neutron flux was substantially uniform and the axial power variations negligible, i.e., less than 2%. The fuel centerline temperature measurement was performed through a 1.5 mm diameter central hole, with potential overestimation of the gas release terms in the low burnup regime). The shutdown was forced by an accidental introduction of air into the water loop, for which fuel rods experienced a shock wave without any deterioration of the instrumentation. For the fuel pellets adopted in the experiments, the surface-to-volume ratio is given as 50 cm^{-1} .

Table 5: Fuel pellet and rod design characteristics of the base-irradiated validation cases employed by SCIANTIX.

		AN3	REGATE	HATAC-C2	CONTACT1
Pellet outer diameter	(mm)	9.053	8.192	0.8193	8.19
Fuel stack length	(mm)	286.0	436.0	3659.4	70 ^a
Pellet density	(%TD)	93.74	94.754	93.984	95
Grain diameter	(μm)	6	13.53 – 16.65	7.05 - 7.99	
²³⁵ U Enrichment	(%)	2.95	4.487	3.138	4.95
Burnup	(MWd/kgUO ₂)	36.84	41.8	40.36	19.39
Average temperature ^b	(K)	830.24	867.61	767.61	951.62

a.

b. The average temperature of the fuel has been estimated from integral simulations employing the TRANSURANUS fuel performance code.

Now that we have established the framework for our final analysis and introduced the experimental cases under consideration, we can proceed to present our results. We will begin by evaluating how our model predicts the mapping of the temperature-burnup space based on the coordinates at which saturation is reached for the different studied cases. Upon examination of Figure 21, it becomes evident that the Baker cases predominantly inhabit a region characterized by low burnups and high temperatures. Here, a steep incline in the incubation time is notable, indicating that saturation at elevated temperatures occurs almost immediately at the onset of irradiation. Moreover, the incubation time appears to decrease exponentially as the temperature is increased. Beyond this high-temperature regime, a slower linear trend emerges, closely accompanied by the Kashibe test cases. As burnup values increase further, reaching substantial levels of irradiation, this linearity begins to diminish, until it ultimately collapses. This observation suggests the existence of a threshold burnup value, located approximately at 77-78 MWd/kgUO₂, beyond which saturation is reached at all temperature values. For what concerns the experimental points, our model anticipates that they will be located in a region dominated by athermal release and not by thermal diffusion. This sits closely in line with what is expected considering their experimental values FGR. Regarding the experimental points, our model predicts their placement in a region primarily governed by athermal release rather than thermal diffusion. This aligns closely with expectations given their experimental values of FGR.

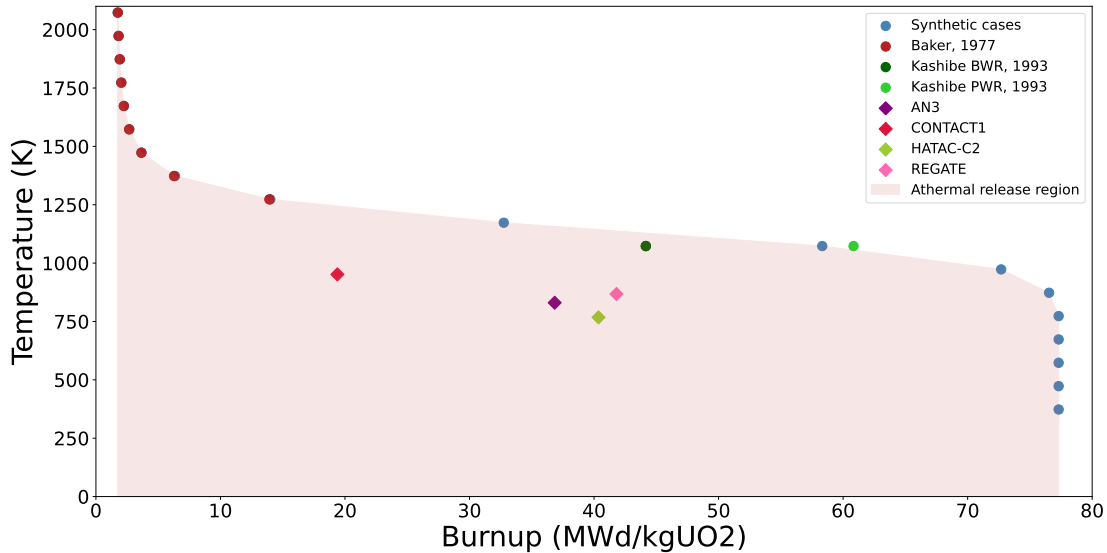


Figure 21: Mapping of the temperature-burnup space based on the coordinates at which grain-boundary saturation is reached for the different studied cases.

Now, let us construct a similar map, delineating the values of temperature and burnup at which fission gas release exceeds the threshold value of 1%, and juxtapose it with the Vitanza criterion, also known as the Halden threshold. Let us recall its expression:

$$T_c = \frac{9800}{\ln\left(\frac{\beta}{0.00567}\right)} \quad (31)$$

where T_c is the rod centerline temperature, expressed in °C, and β is the rod average burnup, expressed in GWd/t_{HM}.

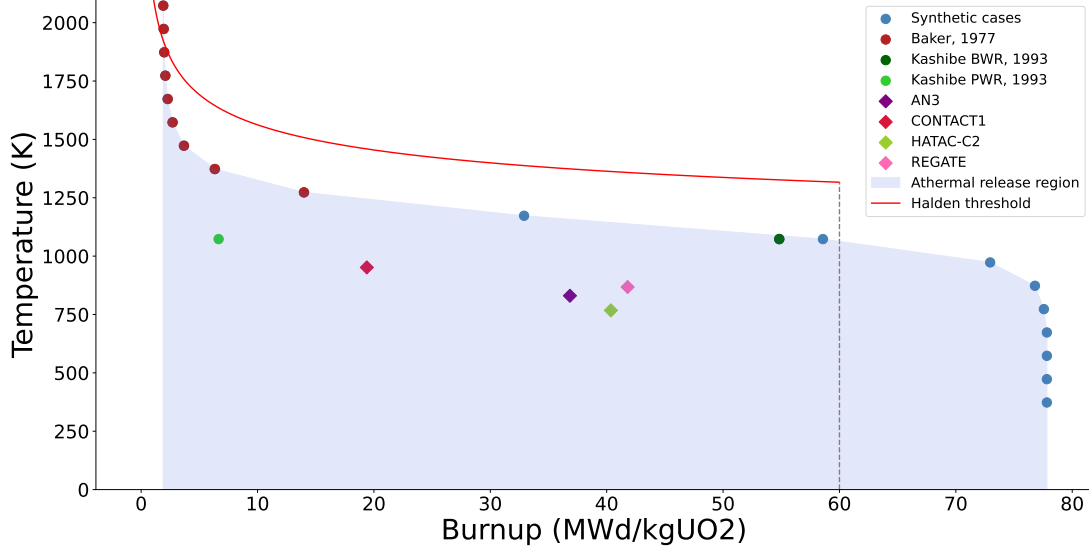


Figure 22: Mapping of the temperature-burnup space based on the coordinates at which fission gas release exceeds 1% for the different studied cases, compared to the Halden threshold.

As depicted in Figure 22, the Halden threshold slightly surpasses the athermal boundary outlined in our mapping, consistently serving as an upper limit for the region of athermal release as defined by our model. This trend persists throughout the entire domain where the Vitanza criterion remains valid, with exceptions found in sections of the graph influenced by the highest temperatures encountered in the Baker cases. This observation aligns with the fact that the Vitanza criterion is formulated based on the fuel centerline temperature, while our investigation focuses on local temperature values. Furthermore, our validation cases were presented in terms of their average temperature, further emphasizing this remark. Once more, all experimental cases under consideration occupy a portion of the T- β space governed by athermal fission gas release. This reaffirms our earlier observation and simultaneously aligns with the experimental data.

Upon comparing Figures 21 and 22, the similarity between the two maps becomes evident, with the only exception of the Kashibe test case under PWR conditions. In this experimental scenario, fission gas release is expected to reach 1% rather early during this irradiation history. In line with our previous discussion, this can be merely ascribed to the peculiar fuel composition of the specimen utilized in this test. Figure 21 demarcates a domain where it is anticipated that grain boundaries will remain unsaturated, thus establishing a discernible physics-based upper limit -applicable at the grain-scale level- within the T- β space where athermal release is anticipated to dominate. Conversely, Figure 22 predicts values of T- β where fission gas release - a quantity that bears relevance at the macroscopic scale level of the fuel rod- is expected not to exceed 1%, providing a more engineering-oriented upper limit for the corresponding region of athermal release. The convergence of these two trends bears significance, as it underscores the juxtaposition between engineering and physical limits, revealing the intrinsic intertwining between the mesoscale and the macroscopic scale.

All the experimental cases, consistent with their empirical data, are predicted to reside within the athermal release region, delineated by both physics-based and engineering-oriented limits. As previously mentioned, these experimental data points were assessed based on average temperatures. The SCIANTIX code operates at the mesoscale in a 0-D manner. Consequently, in the context of integral effect tests, it is not expected that the entire fuel rod will remain below the saturation limit. However, when considering a localized description of fuel behavior, the aforementioned observations remain applicable. Therefore, these maps can serve as a tool for evaluating the predicted region of fission gas release, whether influenced primarily by athermal behavior or thermal diffusion.

This analysis further underscores the significance of a model for athermal release, demonstrating its relevance across a broad range of applications and shedding light on its potential in informing designing both experimental setups and fuel rods. The substantial importance in evaluating fission gas release that an accurate model for athermal release carries is further reiterated, as it plays a crucial role not only in the design, licensing, and operation of nuclear reactors but also in the context of final repositories.

6. Conclusions and Future Developments

In conclusion, in this study, we investigated the importance of incorporating a model for athermal fission gas behaviour in the context of fuel performance applications. In particular, we focused on the athermal fission gas mechanism driven by the presence of open pores structures in the fuel matrix. The as-fabricated porosity in the sintered fuel contributes to a network of open channels along grain edges, essentially providing an easy escape path for gas atoms produced within the fuel grain. The scope of this investigation was to present a physics-based model, built upon the framework established by a mechanistic model in the open literature, developed by Claisse and Van Uffelen, augmenting it with machine-learning techniques. Expanding upon Claisse’s model, we introduced a new quantity, aimed at accounting for the dependency of the real shape of gas flux exiting the fuel grain and including the influence of the grain-edge inclination angle in the diffusion process, and accurately representing the real geometry of our domain.

This quantity, which we called λ_{ath} , was defined as a measure of the real fractional amount of gas flux that exits the fuel grain through the open porosity tunnel. With the scope of computing λ_{ath} we incorporated a wide range of relevant dependencies impacting on geometry (θ, l), fuel composition (P_{fab}), diffusion dynamics (T, S, C_0), and temporal variations (β). A high-fidelity code was employed to numerically solve the gas diffusion equation, providing accurate estimations of λ_{ath} across a wide range of conditions. In order to encapsulate the complex dependencies affecting the athermal release of fission gas diffusing in the fuel grain, whilst ensuring a computational time in line with fuel performance applications, a synthetic dataset generated from the high-fidelity code was used to train a feed-forward neural network. The choice of such a model, among artificial intelligence techniques, was deemed most appropriate for the sake of AI-explainability.

Accompanying this AI-enhance physics-based model for athermal release, in the context of this analysis, semi-empirical models to describe fuel solid fission products swelling and porosity densification were also presented.

Separate effect tests were conducted to assess the performance of SCIANTIX, augmented by the models described in this work, employing the Kashibe and Baker cases as benchmark scenarios. Additionally, we integrated with additional synthetic cases to widen the ranges of temperature and burnup studied. Furthermore, experimental data on fission gas release from base-irradiation cases, used for the integral validation of SCIANTIX, was utilized to further explore the model’s behaviour.

The results of this study, particularly for what concerns fission gas release in base-irradiated scenarios, showed good agreement with experimental data.

This study emphasizes the critical importance of developing a comprehensive athermal release model that encompasses all associated phenomena pertinent to low-temperature operating conditions. It particularly showcases its relevance across diverse applications and highlights its potential in informing the design of both experimental setups and fuel rods.

The use of machine learning techniques to improve a model for fission gas release unraveling the behavior of nuclear fuel in the context of fuel performance application also carries significant implications. Nuclear materials, in general, are frequently required to endure prolonged periods in harsh environments characterized by high radiation levels, transmutation, elevated temperatures, temperature gradients, mechanical stresses, and corrosive coolant conditions. Moreover, these materials exhibit diverse microstructural and chemical compositions, leading to intricate and often non-equilibrium interactions governed by mechanisms yet not fully understood. Machine learning is being progressively employed to address these complex, time-dependent interactions, assisting the development of models and making predictions, often surpassing the accuracy of traditional modeling approaches that focus on isolated parameters [53]. Indeed, traditional empirical and semi-empirical models heavily lean on experimental fits, often sacrificing accuracy in capturing the fundamental physics governing these interdependencies. There is a noticeable trend toward increasingly utilizing machine learning techniques, particularly for atomistic studies (e.g. [54]) tackling nuclear material behaviour under irradiation. Nonetheless, this same approach can be effectively applied in fuel performance applications. By leveraging machine learning to augment physics-based models, there exists a significant potential for enhancing the predictive capabilities of fuel performance codes, without jeopardizing computational efficiency. It is worth reiterating that in this work, we utilized a standalone version of the SCIANTIX code. Therefore, to advance our investigation, integral validation stands as a crucial step, along with exploring methods to enhance the explainability and interpretability of the artificial intelligence techniques employed. This would ensure that our analysis remains robust at the macroscopic level of the entire fuel rod, and strengthen the applicability and physical foundation of the machine learning model utilized.

Moreover, an uncertainty assessment of the models developed in this work, coupled with sensitivity analysis of the newly introduced quantities would also further improve our investigation.

Lastly, to better the performance and accuracy of our estimation of athermal release, additional relevant phenomena could be included. Namely, other mechanisms could possibly affect the fraction of open porosity, especially during transient scenarios at extended burnup, as suggested by the work of Mogensen et al. [55]. One such phenomenon to consider could be fuel micro-cracking [56], which triggers a burst fission gas release effect within the fuel. This mechanism, akin to athermal release, can also be viewed as a form of venting. Consequently, treating these two mechanisms in a combined manner under the broader description of grain boundary venting could be beneficial.

7. Bibliography and citations

References

- [1] R.C. Ewing J. Bruno. Spent nuclear fuel. *Elements*, 2(6):343–349, 2006.
- [2] M. Mogensen, C.T. Walker, I.L.F. Ray, M. Coquerelle. Local fission gas release and swelling in water reactor fuel during slow power transients. *Journal of Nuclear Materials*, 131:162–171, 1985.
- [3] R.J. White, M.O. Tucker. A new fission-gas release model. *Journal of Nuclear Materials*, 118:1–38, 1983.
- [4] A.H. Booth. A method of calculating fission gas diffusion from UO_2 fuel and its application to the X-2-f loop test. Technical report.
- [5] K. Tanaka, K. Maeda, K. Katsuyama, M. Inoue, T. Iwai, Y. Arai. Fission gas release and swelling in uranium-plutonium mixed nitride fuels. *Journal of Nuclear Materials*, 327:77–87, 2004.
- [6] C. Ferry, C. Poinssot, C. Cappelaere, L. Desgranges, C. Jegou, F. Miserque, J.P. Piron, D. Roudil, J. M. Gras. Specific outcomes of the research on the spent fuel long-term evolution in interim dry storage and deep geological disposal. *Journal of Nuclear Materials*, 352:246–253, 2006.
- [7] W. Hering. The KWU fission gas release model for LWR fuel rods. *Journal of Nuclear Materials*, 114:41–49, 1983.
- [8] P.C. Millett. Percolation on grain boundary networks: Application to fission gas release in nuclear fuels. *Computational Materials Science*, 53:31–36, 2012.
- [9] P.C. Millett, M.R. Tonks, S.B. Biner. Grain boundary percolation modeling of fission gas release in oxide fuels. *Journal of Nuclear Materials*, 424:176–182, 2012.
- [10] A. Claisse, P. Van Uffelen. Towards the inclusion of open fabrication porosity in a fission gas release model. *Journal of Nuclear Materials*, 466:351–356, 2015.
- [11] R.J. White. The development of grain-face porosity in irradiated oxide fuel. *Journal of Nuclear Materials*, 325:61–77, 2004.
- [12] D. Pizzocri, T. Barani, L. Luzzi. SCIANITX: A new open source multi-scale code for fission gas behaviour modelling designed for nuclear fuel performance codes. *Journal of Nuclear Materials*, 532:152042, 2000.
- [13] S. Kashibe, K. Une and K. Nogita. Formation and growth of intragranular fission gas bubbles in UO_2 fuels with burnup of 6-83 GWd/t. *Journal of Nuclear Materials*, 206:22–34, 1993.
- [14] C. Baker. The fission gas bubble distribution in uranium dioxide from high temperature irradiation SGHWR fuel pins. *Journal of Nuclear Materials*, 66:283–291, 1977).
- [15] R. The Third RisøFission Gas Project: Bump Test AN3 (CB8-2R). Technical Report Risø-FGP3-AN3, Risø, September 1990.
- [16] J. Killeen and International Atomic Energy Agency. Fuel Modelling at Extended Burnup (FUMEX-II). Technical report, IAEA, 2012.
- [17] M. Bruet, M.L. Pointud, J. Dodelier, P.H. Melin. Contact 1 and 2 experiments: behaviour of PWR fuel rod up to 15000 MWd.tu-1. Technical Report Risø-FGP3-AN4, IAEA, Blackpool, UK, 1980. Specialists’ meeting on fuel element performance computer modelling.

- [18] K.W. Song, K.S. Kim, Y.M. Kim, K.W. Kang, Y.H. Jung. Reduction of the open porosity of UO₂ pellets through pore structure control. *Journal of Nuclear Materials*, 279:253–258, 2000.
- [19] C. Matthews, R Perriot, M.W.D Cooper, C. R. Stanek, D. A. Andersson. Cluster dynamics simulation of xenon diffusion during irradiation in UO₂. *Journal of Nuclear Materials*, 540:152326, 2020.
- [20] The MathWorks Inc. Matlab version: 9.13.0 (r2022b), 2022.
- [21] S. Valin, A. Mocellin, G. Eminent, S. Ravel. Modelling the behaviour of intergranular fission gas during out-of-pile annealing. Technical report, Cadarache, France, 9 2000. Fission Gas Behaviour In Water Reactor Fuels.
- [22] C. Molnar. *Interpretable Machine Learning*. <https://christophm.github.io/interpretable-ml-book/>, 2019. <https://christophm.github.io/interpretable-ml-book/>.
- [23] F.Cappia, D.Pizzocri, A.Schubert, P. Van Uffelen, G. Paperini, D. Pellottiero, R. Macian-Juan, V.V. Rondinella. Critical assessment of the pore size distribution in the rim region of high burnup UO₂ fuels. *Journal of Nuclear Materials*, 480:138–149, 2016.
- [24] D.R. Olander. *Fundamental Aspects of Nuclear Reactor Fuel Elements*. Technical Information Centre, Office of Public Affairs Energy Research and Development Administration, Department of Nuclear Engineering University of California, Berkeley, USA, 1976.
- [25] D. Pizzocri, G. Pastore, T. Barani, A. Magni, L. Luzzi, P. Van Uffelen, S. A. Pitts, A. Alfonsi, J. D. Hales. A model describing intra-granular fission gas behaviour in oxide fuel for advanced engineering tools. *Journal of Nuclear Materials*, 502:323–330, 2018.
- [26] F. Cappia G. Pastore L. Luzzi P. Van Uffelen T. Barani, D. Pizzocri. A model describing intra-granular fission gas behaviour in oxide fuel for advanced engineering tools. *Journal of Nuclear Materials*, 563:153627, 2022.
- [27] J. Spino, A.D. Stalios, H. Santa Cruz, D. Baron. Stereological evolution of the rim structure in PWR-fuels at prolonged irradiation: Dependencies with burn-up and temperature. *Journal of Nuclear Materials*, 354:66–84, 2006.
- [28] M.D. Freshley, D.W. Brite, J.L. Daniel, P.E. Hart. Irradiation-induced densification of UO₂ pellet fuel. *Journal of Nuclear Materials*, 62:138–166, 1976.
- [29] H. Stehle H. Assmann. Thermal and in-reactor densification of UO₂: Mechanisms and experimental results. *Nuclear Engineering and Design*, 48(1):49–67, 1978.
- [30] H.C. Suk, W. Hwang, B.G. Kim, K.S Kim, Y.H. Heo. Improvement of elesim candu fuel performance analysis code. Technical report, IAEA, Pembroke, Ontario, Canada, 5 1992. Technical Committee Meeting on Fission gas release and fuel rod chemistry related to extended burnup.
- [31] I.J. Hastings, L.E. Evans. Densification algorithm for irradiated UO₂ fuel. *Journal of Nuclear Materials*, 62(3-4):217–218, 1979.
- [32] P.A. Jackson, J.A. Turnbull and R.J. White. A description of the ENIGMA Fuel Performance Code. Technical report, IAEA, Vienna, Austria, 9 1989. Technical Committee Meeting on Water Reactor Fuel Element Computer Modelling in Steady-State, Transient and Accident Conditions.
- [33] P. Van Uffelen. *Contribution to the Modelling of Fission Gas Release in Light Water Reactor Fuel*. PhD thesis, Université de Liège, Liège, Belgium, 1 2002.
- [34] V.I. Tarasov, M.S. Veshchunov. Models for fuel porosity evolution in UO₂ under various regimes of reactor operation. *Journal of Nuclear Materials*, 272:65–83, 2014.
- [35] J.B. Ainscough, B.W. Oldfield, J.O. Ware. Isothermal grain growth kinetics in sintered UO₂ pellet. *Journal of Nuclear Materials*, 49:117–128, 1976.
- [36] D. W. Brite, J. L. Daniel, N. C. Davis, M. D. Freshley, P. E. Hart. EEI/EPRI fuel densification project. Final report. UO₂.
- [37] Idaho National Engineering and Environmental Laboratory, BECHTEL BWXT IDAHO, LLC Idaho Falls, Idaho, USA. *SCDAP/RELAP5-3D© CODE MANUAL VOLUME 4: MATPRO - A LIBRARY OF MATERIALS PROPERTIES FOR LIGHT-WATER-REACTOR ACCIDENT ANALYSIS*.

- [38] M. Lippens. Densification of UO_2 - PuO_2 fuel. *Journal of Nuclear Materials*, 81:99–105, 1979.
- [39] L. Caillot, P.P. Malgouyres, F. Souchon, M.J. Gotta, D. Warin, A. Chotard, J.C. Couty. Thermal and in-pile densification of MOX fuels: some recent results. Technical report, IAEA, Newby Bridge, Windermere, UK, 7 1995. Technical Committee Meeting on Recycling of Plutonium and Uranium in Water Reactor Fuel.
- [40] B.H. Lee, Y.H. Koo, H.K. Joo, Y.W. Lee, D.S. Sohn. Irradiation test of MOX fuel in the halden reactor during the first cycle and its analysis with a computer code cosmos. Technical report, Korea Atomic Energy Research Institute, Newby Bridge, Windermere, UK, 10 2001. Proceedings of the Korean Nuclear Society Autumn Meeting.
- [41] S. Koizumi, H. Umehara, Y. Wakashima. Study on fission gas release from high burnup fuel. Technical report, Studsvik, Sweden, 6 1990. Technical Committee Meeting on fuel performance at high burnup for water reactors.
- [42] K. Une, K. Nogita, S. Kashibe, M. Imamura. Microstructural change and its influence on fission gas release in high burnup UO_2 fuel. *Journal of Nuclear Materials*, 188:65–72, 1992.
- [43] J.O. Barner, M.E. Cunningham, M.D. Freshley, D.D. Lanning. High Burnup Effects Program - Final report. Technical report, 4 1990. DOE/NE/34046-1 [HBEP-61 (3P27)].
- [44] L.K. Aagesen, D. Schwen, M.R. Tonks, Y. Zhang. Phase-field modeling of fission gas bubble growth on grain boundaries and triple junctions in UO_2 nuclear fuel. *Journal of Nuclear Materials*, 161:35–45, 2019.
- [45] C. Vitanza, U. Graziani, N.T. Førdestrømmen, K. O. Vilpponen. Fission gas release from in-pile pressure measurements. Technical report, Loen, Norway, 6 1978.
- [46] R.J. White, S.B. Fisher, P.M.A. Cook, R. Stratton, C.T. Walker, I.D. Palmer. Measurement and analysis of fission gas release from BNFL's SBR MOX fuel. *Journal of Nuclear Materials*, 288(1):43–56, 2001.
- [47] R.L. Williamson, K.A. Gamble, D.M. Perez, S.R. Novascone, G. Pastore, R.J. Gardner, J.D. Hales, W. Liu, A. Mai. Validating the BISON fuel performance code to integral LWR experiments. *Nuclear Engineering and Design*, 301:232–244, 2016.
- [48] Y.H. Koo, B.H. Lee, D.S. Sohn. COSMOS: A computer code for the analysis of LWR UO_2 and MOX fuel rod. *Nuclear Engineering and Technology*, 30(6):541–554, 1998.
- [49] Y.H. Koo, B.H. Lee, D.S. Sohn. Analysis of fission gas release and gaseous swelling in UO_2 fuel under the effect of external restraint. *Journal of Nuclear Materials*, 280(1):86–98, 2000.
- [50] G. Khvostov, V. Novikov, A. Medvedev, S. Bogatyr. Analysis of fission gas release and gaseous swelling in UO_2 fuel under the effect of external restraint. 10 2005. Conference: 2005 Water Reactor Fuel Performance Meeting.
- [51] T. Kogai. Modelling of fission gas release and gaseous swelling of light water reactor fuels. *Journal of Nuclear Materials*, 244(2):131–140, 1997.
- [52] T. Barani, E. Bruschi, D. Pizzocri, G. Pastore, P. Van Uffelen, R.L. Williamson, L. Luzzi. Analysis of transient fission gas behaviour in oxide fuel using BISON and TRANSURANUS. *Journal of Nuclear Materials*, 486:96–110, 2017.
- [53] D. Morgan, G. Pilania, A. Couet, B.P. Uberuaga, C. Sun, J. Li. Machine learning in nuclear materials research. *Current Opinion in Solid State and Materials Science*, 26(2):100975, 2022.
- [54] K. Kobayashi, M. Okumura, H. Nakamura, M. Itakura, M. Machida, M.W.D. Cooper. Machine learning molecular dynamics simulations toward exploration of high-temperature properties of nuclear fuel materials: case study of thorium dioxide. *Scientific Reports*, 12:9808, 2022.
- [55] M. Mogensen, C. Bagger, H. Toftegaard, P. Knudsen, C.T. Walker. Observations of athermal gas release from water-reactor fuel at extended burnup. *Journal of Nuclear Materials*, 202:199–209, 1993.
- [56] T. Barani, E. Bruschi, D. Pizzocri, G. Pastore, P. Van Uffelen, R.L. Williamson, L. Luzzi. Analysis of transient fission gas behaviour in oxide fuel using BISON and TRANSURANUS. *Journal of Nuclear Materials*, 486:96–110, 1993.

A. Analytical solution of the diffusion equation

The motion of gas atoms in a 2-D representation of the grain follows an inhomogeneous diffusion of the kind:

$$\frac{\partial c(x, y, t)}{\partial t} = \nabla \cdot \left(D \nabla c(x, y, t) \right) + S \quad (32)$$

where

- $c(x, y, t)$ (at m^{-3}) is the gas concentration
- D ($\text{m}^2 \text{s}^{-1}$) is the gas diffusivity
- S (at $\text{m}^{-3} \text{s}^{-1}$) is the gas generation rate

with the initial condition:

$$c(x, y, t = 0) = c_0 \quad (33)$$

and *boundary conditions*:

$$\begin{cases} c(x, y \in \partial A, t) = 0 \\ \frac{\partial c}{\partial x} \Big|_{x=0} = 0 \\ \frac{\partial c}{\partial y} \Big|_{y=0} = 0 \end{cases} \quad (34)$$

In general, our domain is a rhombus of side $\frac{l}{2}$ with a vertex angle θ as shown in Figure 4. Therefore, the y coordinate, with respect to a Cartesian coordinate system, will be always expressed as a function of θ , as shown in Figure 23. Moreover, the spatial boundary condition on surface S_2 will be also defined based on the position of the points lying on it and therefore as a function of both coordinates. The inherent complexity arising from this unique domain structure hinders solving Equation 32 analytically within the real non-orthogonal geometry of the grain.

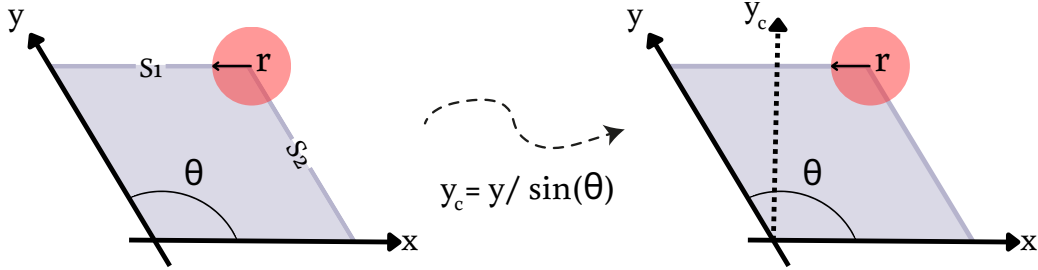


Figure 23: Comparison of the representation of our domain in a non-orthogonal reference system, loyal to the grain geometry, and the Cartesian reference system.

To simplify matters, let's begin by analyzing the most straightforward geometric scenario, where $\theta = \frac{\pi}{2}$, resulting in a square domain. In this configuration, the reference system that tracks the inclination of the grain edges aligns with the Cartesian coordinate system.

We'll first use separation of variables to express $c(x, y, t)$ as a sum of spatial and temporal eigenfunctions. Let's assume:

$$c(x, y, t) = \sum_{n=1}^{\infty} a_n(t) \psi_n(x, y) \quad (35)$$

where $a_n(t)$ are the time-dependent coefficients and $\psi_n(x, y)$ are the spatial eigenfunctions corresponding to the eigenvalues ω_n .

Substituting this into Equation 32, we get:

$$\sum_{n=1}^{\infty} \frac{\partial a_n(t)}{\partial t} \psi_n(x, y) = D \sum_{n=1}^{\infty} \nabla^2 (a_n(t) \psi_n(x, y)) + S \quad (36)$$

Since the spatial eigenfunctions are independent of time, we can bring them out of the spatial derivatives:

$$\sum_{n=1}^{\infty} \frac{\partial a_n(t)}{\partial t} \psi_n(x, y) = D \sum_{n=1}^{\infty} \psi_n(x, y) \nabla^2 a_n(t) + S \quad (37)$$

Now, dividing both sides by $\psi_n(x, y)$ and rearranging terms, we get:

$$\frac{1}{D} \sum_{n=1}^{\infty} \frac{1}{a_n(t)} \frac{da_n}{dt} = \frac{\nabla^2 \psi_n}{\psi_n} + \frac{S}{D} \quad (38)$$

Since the left side depends only on time and the right side depends only on space, they must be equal to a constant. Let's denote this constant as $-\omega_n^2$:

$$\frac{1}{D} \sum_{n=1}^{\infty} \frac{1}{a_n(t)} \frac{da_n}{dt} = -\omega_n^2 = \frac{\nabla^2 \psi_n}{\psi_n} + \frac{S}{D} \quad (39)$$

Now, we have separated the variables, and we have an eigenvalue problem for both time and space. Solving the temporal term we immediately get:

$$\frac{1}{D} \frac{d^2 a_n}{dt^2} = -\omega_n^2 a_n + \frac{S}{D} \quad (40)$$

The general solution is:

$$a_n(t) = A e^{-\omega_n^2 D t} + B e^{\omega_n^2 D t} + \frac{S}{\omega_n^2 D} \quad (41)$$

where A and B are constants.

The constants A and B can be determined using the initial condition reported in Equation 33. Substituting $t = 0$ into the solution and equating it to c_0 , we can solve for A and B .

while for what concerns the spacial solution we must separate once again: Let us say that:

$$\psi_m(x, t) = \xi_n(x) \zeta_m(y) \quad (42)$$

where n and m are positive integers.

Hence:

$$\underbrace{\frac{1}{\xi_m(x)} \frac{d^2 \xi_m(x)}{dx^2}}_{-\alpha_m^2} + \underbrace{\frac{1}{\zeta_m(y)} \frac{d^2 \zeta_m(y)}{dy^2}}_{-\beta_m^2} = -\text{constant} \quad (43)$$

We get a system of two equations:

$$\begin{cases} \frac{1}{\xi_n(x)} \frac{d^2 \xi_n(x)}{dx^2} = -\alpha_n^2 \\ \frac{1}{\zeta_m(y)} \frac{d^2 \zeta_m(y)}{dy^2} = -\beta_m^2 \end{cases} \quad (44)$$

which stem solutions of the kind:

$$\begin{cases} \xi_n(x) = \cos(\alpha_n x) + \sin(\alpha_n x) \\ \zeta_m(y) = \cos(\beta_m y) + \sin(\beta_m y) \end{cases} \quad (45)$$

In order to satisfy the symmetry condition with respect to the x and y axes, we can immediately disregard the sinusoidal terms and re-name the constants:

$$\begin{cases} \xi_n(x) = \cos(\alpha_n x) \\ \zeta_m(y) = \cos(\beta_m y) \end{cases} \quad (46)$$

So our general solution will be of the form:

$$\begin{aligned} c(x, y, t) &= \sum_{n=1}^{\infty} a_n(t) \psi_n(x, y) \\ &= \sum_{n,m=1}^{\infty} a_n(t) \cos(\alpha_n x) \cos(\beta_m y) \end{aligned} \quad (47)$$

Having already enforced the initial condition on the temporal term of the diffusion equation, let us enforce the boundary conditions which ensure that the gas concentration at the edge of our domain is null.

$$\begin{cases} c(x = \frac{l}{2}, y, t) = 0 \iff \xi(x = \frac{l}{2}) = 0 \\ c(x, y = \frac{l}{2}, t) = 0 \iff \zeta(y = \frac{l}{2}) = 0 \end{cases} \quad (48)$$

Which means that:

$$\begin{cases} \cos(\alpha \frac{l}{2}) = 0 \\ \cos(\beta \frac{l}{2}) = 0 \end{cases} \quad (49)$$

This is satisfied only if the eigenvalues of the two spatial eigenfunctions are of the kind:

$$\begin{cases} \alpha_n = \frac{\pi}{l}(2n+1) \quad n \in N \\ \beta_m = \frac{\pi}{l}(2m+1) \quad m \in N \end{cases} \quad (50)$$

At this point, we can recall, once again, the definition of our corrective factor as previously introduced in equation 6:

$$\lambda_{\text{ath}} := \frac{\langle \varphi^{\text{out}} \rangle_{\text{op}}}{\langle \varphi^{\text{out}} \rangle_{\text{tot}}} \quad (51)$$

where:

$$\begin{cases} \langle \varphi^{\text{out}} \rangle_{\text{op}} = \frac{2}{r} \int_r^{\frac{l}{2}} -D \nabla c(x, y, t) dx dy \\ \langle \varphi^{\text{out}} \rangle_{\text{tot}} = \frac{1}{l} \int_l -D \nabla c(x, y, t) dx dy \end{cases} \quad (52)$$

To simplify our computation we can consider to evaluate our corrective factor only on one side, for instance, let us consider the top edge. In this case λ_{ath} can be simply computed as:

$$\lambda_{\text{ath}} = \frac{\frac{1}{r} \int_{\frac{l}{2}-r}^{\frac{l}{2}} -D \frac{\partial c(x, y, t)}{\partial x} \Big|_{y=\frac{l}{2}} dx}{\frac{2}{l} \int_0^{\frac{l}{2}} -D \frac{\partial c(x, y, t)}{\partial x} \Big|_{y=\frac{l}{2}} dx} \quad (53)$$

Enforcing the solution found in equation 47 and simplifying:

$$\lambda_{\text{ath}} = \frac{\frac{1}{r} \sum_{n=1}^{\infty} a_n(t) \alpha_n \int_{\frac{l}{2}-r}^{\frac{l}{2}} \sin(\alpha_n x) dx}{\frac{2}{l} \sum_{n=1}^{\infty} a_n(t) \alpha_n \int_0^{\frac{l}{2}} \sin(\alpha_n x) dx} \quad (54)$$

Using the orthogonality property of sine functions:

$$\int_0^{\frac{l}{2}} \sin(\alpha_n x) \sin(\alpha_m x) dx = \frac{l}{4} \delta_{nm} \quad (55)$$

where δ_{nm} is the Kronecker delta. Substituting this into λ_{ath} , we get:

$$\begin{aligned} \lambda_{\text{ath}} &= \frac{\frac{1}{r} \sum_{n=1}^{\infty} a_n(t) \alpha_n \left(-\frac{1}{\alpha_n} \cos\left(\frac{\pi}{2}\right) + \frac{1}{\alpha_n} \cos\left(\frac{\pi}{2} - \alpha_n r\right) \right)}{\frac{2}{l} \sum_{n=1}^{\infty} a_n(t) \alpha_n \left(-\frac{1}{\alpha_n} \cos\left(\frac{\pi}{2}\right) + \frac{1}{\alpha_n} \right)} \\ &= \frac{\frac{1}{r} \sum_{n=1}^{\infty} a_n(t) \alpha_n \left(-\cos\left(\frac{\pi}{2} - \alpha_n r\right) \right)}{\frac{2}{l} \sum_{n=1}^{\infty} a_n(t) \left(-\cos\left(\frac{\pi}{2}\right) + 1 \right)} \\ &= \frac{\sum_{n=1}^{\infty} a_n(t) \left(\cos\left(\frac{\pi}{2} - \alpha_n r\right) \right)}{\sum_{n=1}^{\infty} a_n(t)} \\ &= \frac{\sum_{n=1}^{\infty} a_n(t) \sin(\alpha_n r)}{\sum_{n=1}^{\infty} a_n(t)} \\ &= \frac{\sum_{n=1}^{\infty} a_n(t) \sin\left(\frac{\pi}{l}(2n+1)r\right)}{\sum_{n=1}^{\infty} a_n(t)} \end{aligned} \quad (56)$$

Computing this ratio proves to be notably burdensome even in the simplest geometry we can consider - disregarding the dependency on the grain-edge inclination angle. This analytical derivation further reinforces and justifies the use of a numerical techniques to compute the athermal venting correction factor λ_{ath} as detailed in Section 2.

Abstract in lingua italiana

Il crescente interesse nei confronti dei fenomeni a basse temperature richiede una dettagliata analisi del comportamento atermico dei gas di fissione. Tale studio riveste particolare importanza per i reattori operanti in condizioni di bassa temperatura, tra cui determinati modelli di Reattori Modulari Compatti e reattori a neutroni veloci che impiegano combustibili ad alta conducibilità termica, come ad esempio i combustibili a base di nitruri. Inoltre, le sue implicazioni si estendono al contesto delle condizioni di stoccaggio del combustibile esaurito. Nel presente lavoro viene presentato un modello fisico potenziato da tecniche di intelligenza artificiale, finalizzato ad approfondire la comprensione del comportamento del gas di fissione atermico. Tale modello estende modelli meccanicistici tradizionalmente disponibili nella letteratura. Il concetto di rilascio atermico, definito come la frazione di gas espulso dal combustibile attraverso la sua porosità aperta, viene considerato mediante la risoluzione della diffusione del gas all'interno del grano di combustibile, valutando il gradiente di concentrazione nelle vicinanze dei bordi del grano. Il risultato di questa analisi è incluso nel codice SCIANTIX grazie all'implementazione di una rete neurale dedicata. Tale rete mira a catturare le intricate dipendenze che influenzano il rilascio atermico, assicurando nel contempo un tempo computazionale congruente con le esigenze applicative nel campo dei codici di prestazione del combustibile nucleare. Inoltre, all'interno di questa ricerca, sono stati incorporati modelli semi-empirici atti a descrivere i fenomeni di rigonfiamento da prodotti di fissione solidi e di densificazione del combustibile, entrambi rilevanti in condizioni di bassa temperatura. La capacità predittiva del modello è stata testata utilizzando dati e casi sperimentali disponibili nella letteratura scientifica.

Parole chiave: applicazioni a bassa temperatura, rilascio di gas di fissione, comportamento atermico di gas di fissione, SCIANTIX, intelligenza artificiale, rete neurale

Acknowledgements



This work has received funding from the Euratom research and training programme 2021-2027 through the OperaHPC project under grant agreement no 101061453.



This work has been partially supported by the ENEN2plus project (HORIZON-EUROATOM-2021-NRT-01-13 101061677) funded by the European Union.